IMPACT performance as an imaging DOAS instrument during the CINDI-3 Campaign

Master Thesis

Sponsored by:

Institute of Environmental Physics, Bremen

Submitted to:

Department of Postgraduate Programme Environmental Physics, University of Bremen

Written by:

Name:	Attahir Umar Mainika
Matriculation number:	6221564
Date:	October 24, 2024

Supervisor/Examiner: **PD Dr. Andreas Richter**

Second Examiner: **Prof. Dr. Mihalis Vrekoussis**

pep

Universität Bremen

Nachname	Attahir Umar	Matrikelnr.	6221564
Vorname	Mainika		

A) Eigenständigkeitserklärung

Ich versichere, dass ich die vorliegende Arbeit selbstständig verfasst und keine anderen als die angegebenen Quellen und Hilfsmittel verwendet habe. Alle Teile meiner Arbeit, die wortwörtlich oder dem Sinn nach anderen Werken entnommen sind, wurden unter Angabe der Quelle kenntlich gemacht. Gleiches gilt auch für Zeichnungen, Skizzen, bildliche Darstellungen sowie für Quellen aus dem Internet, dazu zählen auch KI-basierte Anwendungen oder Werkzeuge. Die Arbeit wurde in gleicher oder ähnlicher Form noch nicht als Prüfungsleistung eingereicht. Die elektronische Fassung der Arbeit stimmt mit der gedruckten Version überein. Mir ist bewusst, dass wahrheitswidrige Angaben als Täuschung behandelt werden.

☒ Ich habe KI-basierte Anwendungen und/oder Werkzeuge genutzt und diese im Anhang "Nutzung KI basierte Anwendungen" dokumentiert.

B) Erklärung zur Veröffentlichung von Bachelor- oder Masterarbeiten

Die Abschlussarbeit wird zwei Jahre nach Studienabschluss dem Archiv der Universität Bremen zur dauerhaften Archivierung angeboten. Archiviert werden:

1) Masterarbeiten mit lokalem oder regionalem Bezug sowie pro Studienfach und Studienjahr 10 % aller Abschlussarbeiten
2) Bachelorarbeiten des jeweils ersten und letzten Bachelorabschlusses pro Studienfach und Jahr.

☒ Ich bin damit einverstanden, dass meine Abschlussarbeit im Universitätsarchiv für wissenschaftliche Zwecke von Dritten eingesehen werden darf.

☒ Ich bin damit einverstanden, dass meine Abschlussarbeit nach 30 Jahren (gem. §7 Abs. 2 BremArchivG) im Universitätsarchiv für wissenschaftliche Zwecke von Dritten eingesehen werden darf.

☐ Ich bin nicht damit einverstanden, dass meine Abschlussarbeit im Universitätsarchiv für wissenschaftliche Zwecke von Dritten eingesehen werden darf.

C) Einverständniserklärung zur Überprüfung der elektronischen Fassung der Bachelorarbeit / Masterarbeit durch Plagiatssoftware

Eingereichte Arbeiten können nach § 18 des Allgemeinen Teil der Bachelor- bzw. der Master-prüfungsordnungen der Universität Bremen mit qualifizierter Software auf Plagiatsvorwürfe untersucht werden.
Zum Zweck der Überprüfung auf Plagiate erfolgt das Hochladen auf den Server der von der Universität Bremen aktuell genutzten Plagiatssoftware.

☒ Ich bin damit einverstanden, dass die von mir vorgelegte und verfasste Arbeit zum oben genannten Zweck dauerhaft auf dem externen Server der aktuell von der Universität Bremen genutzten Plagiatssoftware, in einer institutionseigenen Bibliothek (Zugriff nur durch die Universität Bremen), gespeichert wird.

☐ Ich bin nicht damit einverstanden, dass die von mir vorgelegte und verfasste Arbeit zum o.g. Zweck dauerhaft auf dem externen Server der aktuell von der Universität Bremen genutzten Plagiatssoftware, in einer institutionseigenen Bibliothek (Zugriff nur durch die Universität Bremen), gespeichert wird.

24.10.2024
_____   _____
Datum   Unterschrift

Dedication

This thesis is dedicated to Maimuna Ummi Salis, my greatest motivation throughout this journey.

Acknowledgements

Table of Contents

List of Figures

List of Tables

List of acronyms

AMF	Air Mass Factor
CCD	Coupled Charged Detector
CESAR	Cabauw Experimental Site for Atmospheric Research
CINDI-3	Cabauw Intercomparison Campaign of Nitrogen Dioxide Measuring Instruments
DOAS	Differential Optical Absorption Spectroscopy
DSCD	Differential Slant Column Densities
FOV	Field of View
FWHM	Full Width at Half Maximum
Hg-Cd	Mercury-Cadmium
IMPACT	Imaging MapPer for AtmospheriC ObservaTions
IR	Infrared
ISRF	Instrumental Spectral Response Function
IUPB	Institut für Umweltphysik Bremen
KNMI	Koninklijk Nederlands Meteorologisch Instituut
MAX-DOAS	Multi-Axis DOAS
RMS	Root Mean Square
SC	Slant Column
SZA	Solar Zenith Angles
UTC	Universal Time Coordinates
UV	Ultraviolet
VC	Vertical Column
VOCs	Volatile Organic Compounds

1 Introduction

The Earth's atmosphere has naturally evolved to support life and other various natural processes, as reflected in the saying, "*and We made the sky a protected ceiling…*" (Qur'an 21:32). Numerous atmospheric processes, both human-induced and natural, occur on relatively small scales, often affecting several square kilometres and disrupting the planet's ecosystem. This interplay, combined with modern scientific theories, has piqued the interest of climatologists in studying long-term weather patterns, meteorologists in developing forecasting methods, and atmospheric scientists in examining the Earth's atmosphere and its diverse physical processes. Consequently, high spatial resolution measurements of geophysical parameters have become a focal point of scientific inquiry. Such measurements can only be achieved with instruments of exceptional precision.

Despite their low concentrations, trace gases have a significant overall effect on the chemistry of the troposphere. For example, when volatile organic compounds (VOCs) such as benzene are released into the atmosphere from sources such as vehicle emissions, industrial processes, and natural vegetation, they undergo photochemical reactions in the presence of sunlight. This process involves the interaction of VOCs with oxides of nitrogen, leading to the production of O_3 at the tropospheric level. The term **D**ifferential **O**ptical **A**bsorption **S**pectroscopy (**DOAS**) was first used by (Perner, et al., 1976) and (Platt, Perner, & Pätz, 1979) to describe a technique for measuring trace gases in the atmosphere using artificial light sources (Active DOAS). Over time, the utilisation of solar radiation among others (Passive DOAS techniques) has been improved and expanded to include off-axis (1-D) and 2-D pointing instruments, as well as 3-D multi-axis DOAS (MAX-DOAS).

In the summer of 2016, researchers at the **I**nstitut für **U**mwelt**p**hysik (**IUP**), Bremen developed and deployed a novel imaging instrument for the second **C**abauw **I**ntercomparison campaign of **N**itrogen **D**ioxide measuring **I**nstruments (**CINDI**-2). This instrument, capable of full azimuthal pointing (360°) with a large vertical field of view (~41°), enables high spatial and temporal resolution retrieval of nitrogen dioxide (NO_2) profiles and is the focus of this work.

1.1 Motivation

Like CINDI-3, the CINDI-2 campaign held at the **C**abauw **E**xperimental **S**ite for **A**tmospheric **R**esearch (**CESAR**) from August 25 to October 7, 2016 was primarily to intercompare the latest generation of ground-based remote sensing and in situ air quality instruments. The **E**uropean **S**pace **A**gency's (**ESA**) interest in such inter-calibration activities stems from the ongoing development of several UV-visible space missions aimed at monitoring air quality, including the Copernicus Sentinel 5 Precursor (S5P) satellite launched in October 2017, as well as future Sentinel 4 and 5 satellites (Kreher, et al., 2020). IUP Bremen

Similar to other instruments, the participation of **IMPACT** (**I**maging **M**ap**P**er for **A**tmospheri**C** Observa**T**ions) was centred on assessing the ability of the instrument to retrieve consistent geophysical quantities, including slant columns of nitrogen dioxide (NO_2), oxygen dimer (O_4), water vapour (H_2O) and ozone (O_3) while adhering to controlled measurement protocols and retrieval settings. However, certain on-site enhancements to the instrument have limited its overall contribution to the campaign. This work is closely aligned with the overarching goal of CINDI-3, which was to improve the accuracy and reliability of atmospheric measurements through rigorous intercomparison and validation processes, thereby supporting the advancement of satellite-based air quality monitoring as discussed in Chapter 40. The scope of this work encompasses the following:

- A concise overview of the physics and chemistry governing the Earth's atmosphere and its interaction with radiation.
- A discussion of the methods and techniques employed in atmospheric measurements.
- Characterisation and optimisation of the instrument.
- Calibration activities conducted before and during the CINDI-3 campaign.
- Comprehensive analysis and comparison of the IMPACT instrument with the IUP Bremen **M**ulti-**A**xis **DOAS** (**MAX-DOAS**) instrument.
- Presentation of the results from multiple full hemispheric scans conducted hourly.
- A summary and outlook for future research directions.

2   Physics and Chemistry of the Atmosphere

Characterised by its vertical structure, composition, and interactions with solar radiation, the Earth's atmosphere is a complex and dynamic system. It consists of several layers, including the troposphere, stratosphere, mesosphere, thermosphere, and exosphere, each with distinct temperature profiles and gas compositions as shown in Fig. 2.1.
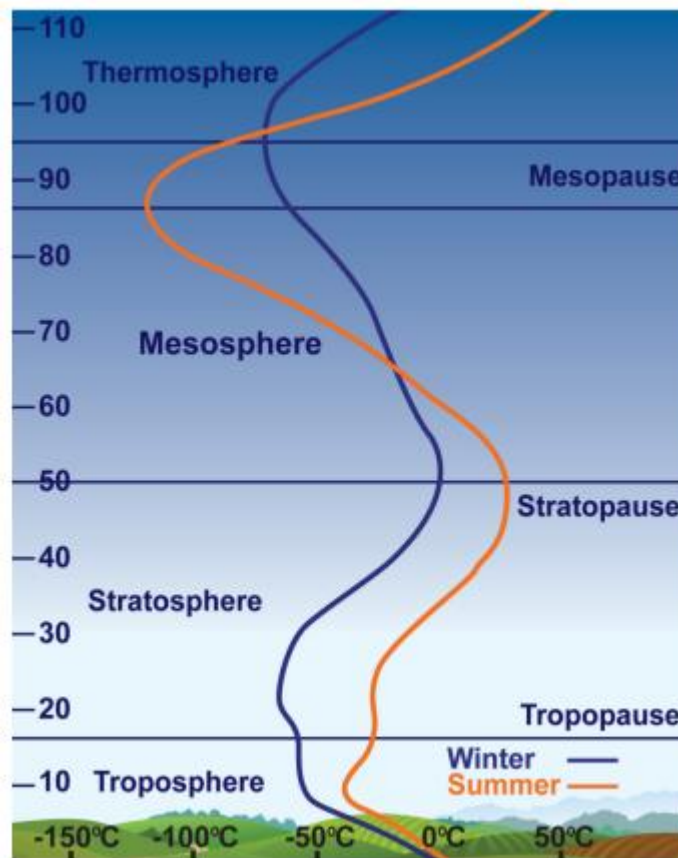
Fig. 2.1: Vertical structure of the atmosphere: temperature profiles in summer (orange line) and winter (blue line), (Vaquer, 2015).

The atmosphere plays a vital role in safeguarding the Earth's surface from high-energy solar radiation. Depending on the wavelength, solar radiation can be reflected, absorbed, or transmitted by the atmosphere. For example, harmful ultraviolet (UV) radiation, which poses risks to human health, is primarily absorbed by the ozone layer located in the stratosphere as illustrated in Fig. 2.2. On the other hand, visible light, essential for photosynthesis and oxygen production in plants, is transmitted to the troposphere. However, this transmitted radiation is subsequently trapped by atmospheric gases

through processes of absorption and scattering, leading to an increase in surface temperatures a phenomenon known as the greenhouse effect.
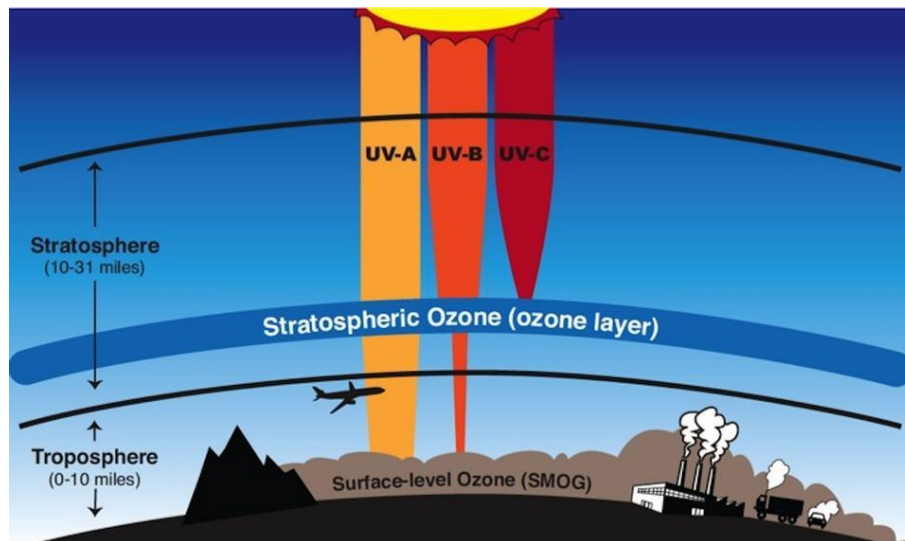
Fig. 2.2: Illustration of interaction of radiation with atmosphere, (NASA, 2024).

While the greenhouse effect is essential for creating a habitable environment on Earth, it also influences the planet's radiative heat budget, thereby altering the balance of Earth's ecosystems. This phenomenon occurs as greenhouse gases trap heat in the atmosphere, which can lead to changes in temperature and climate patterns.

The troposphere is the naturally turbulent layer where weather systems circulate air masses and contain nearly all components of the atmosphere. It primarily comprises of nitrogen (78%), oxygen (21%), argon (1%) and less than 1% trace gases such as carbon dioxide, water vapour and O_3 which are present at very low concentrations

Table 2.1) but have a large impact on the atmospheric processes.

Table 2.1: Current Atmospheric Composition: Bulk (green) and trace (grey) amount.

Constituent	Molecular weight [gmol^{-1}]	Volume mixing Fraction in dry air
Nitrogen (N$_2$)	28.016	78.08%
Oxygen (O$_2$)	32.00	20.95%
Argon (Ar)	39.94	0.93%
Neon (Ne)	20.18	18 ppm
Helium (He)	4.00	5 ppm
Krypton (Kr)	83.70	1 ppm

Hydrogen (H$_2$)	2.02	0.5 ppm
Nitrous oxide (N$_2$O)	44.01	0.3 ppm
Nitrogen species(NO$_y$)	-	10 ppt - 1 ppm
Formaldehyde (CH$_2$O)	30.01	0.1 - 1 ppb
Water vapour (H$_2$O)	18.02	0 - 0.04%
Carbon Dioxide (CO$_2$)	44.01	420 ppm
Ozone (O$_3$)	48.00	0 - 12 ppm

2.1 Atmospheric NO$_x$

Unlike many trace gases, NO$_x$ (NO$_2$ and NO) are stratospheric and tropospheric gases emitted by both natural and anthropogenic sources. They tend to convert into one another rapidly.   In the stratosphere, NO is formed from a rather inert dinitrogen monoxide (N$_2$O) molecule when struck by a singlet oxygen atom (Equation 2.1) resulting in the production of NO which is an O$_3$ depletion substance (ODS).

$$N_2O + O \cdot \rightarrow 2NO$$ Equation 2.1

The impact of O$_3$ on the environment varies significantly depending on its location within the Earth's atmosphere. In the stratosphere, O$_3$ acts as a protective layer, shielding life on earth from harmful UV radiation, as illustrated in Fig. 2.2. However, the release of certain chemicals, particularly halogens, like chlorofluorocarbons (CCl$_3$F), by industrial activities and NO by jet engines, poses a serious threat to the ozone layer.

Although CFCs are produced in the troposphere, these long-lived and stable organic compounds eventually migrate to the stratosphere. They are broken down there by high-energy UV radiation, which releases chlorine radicals. These chlorine radicals participate in a process known as catalytic ozone destruction, where they continuously destroy O$_3$ molecules as they reform.

$$CCl_3F + hv \rightarrow CCl_2F + Cl \cdot$$ Equation 2.2
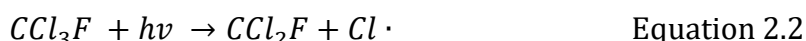
The NO produced reacts with O$_3$ to form NO$_2$, as shown in Equation 2.3. This NO$_2$ which is also a radical then reacts with another ozone to regenerate the NO radical, as illustrated in Equation 2.4. Together, these reactions contribute to the overall process of ozone depletion, which is summarised in Equation 2.5. The Cl $\cdot$ produced in Equation 2.2, undergoes a similar process of ozone depletion, (Revell, et al., 2012).

$$NO + O_3 \rightarrow NO_2 + O_2 \qquad \text{Equation 2.3}$$

$$NO_2 + O_3 \rightarrow NO + 2O_2 \qquad \text{Equation 2.4}$$

$$2O_3 \rightarrow 3O_2 \qquad \text{Equation 2.5}$$
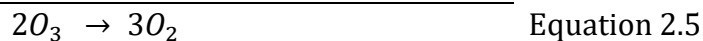
In the troposphere, soil emissions, lightning, and fires are the major natural sources of NO_2 whereas industries, transportation, agriculture and energy production occupy the anthropogenic sources. NO is primarily formed by the combination of nitrogen and oxygen at high temperatures in combustion engines as shown in Equation 2.6 which is then converted to NO_2 as shown in Equation 2.7.

$$N_2 + O_2 \rightarrow 2NO \qquad \text{Equation 2.6}$$

$$2NO + O_2 \rightarrow 2NO_2 \qquad \text{Equation 2.7}$$

While NO_2 causes some types of respiratory diseases which makes it very relevant for health it occupies the background of O_3 chemistry, the formation of secondary pollutants e.g. (HNO_3), which contributes to acidification of rain and water bodies and ozone smog formation during photochemical reactions in the presence of VOCs.

$$NO_2 + h\nu \rightarrow NO + O \cdot \qquad \text{Equation 2.8}$$

$$NO + O_3 \rightarrow NO_2 + O_2 \qquad \text{Equation 2.9}$$

$$O \cdot + O_2 + M \rightarrow O_3 + M \qquad \text{Equation 2.10}$$

When NO_2 is photolysed to NO and atomic oxygen by electromagnetic radiation of energy, $E = h\nu$ (product of Planck's constant, h, and the frequency, v) as shown in Equation 2.8, the NO depletes O_3 to form NO_2 back as shown in Equation 2.10. In contrast, the atomic oxygen results in a temporary O_3 formation in the presence of a non-reactive species (inert gases), M as shown in the reaction. It stabilises the O_3 from falling back to O and O_2, by absorbing the excess energy of the reaction. These equations called Leighton's equilibrium or Do Nothing cycle explain the relationship between NO, NO_2 and O_3 in the troposphere.

However, in the presence of VOCs, the Leighton cycle is suppressed by substituting the O_3 in Equation 2.9 with a VOC as shown in Equation 2.11. This alteration leads to an increase in the background concentration of O_3 in the atmosphere, contributing to the formation of smog. VOC also oxidised in the presence of NO_x which leads to the formation of other complex organic compounds.

$$NO + RO_2 \rightarrow NO_2 + RO_2 \hspace{3cm} \text{Equation 2.11}$$

In the formation of nitrate radical ($NO_3\cdot$) through O_3 removal by NO_2, the radical is further converted to dinitrogen pentoxide (N_2O_5), but due to the rapid photolysis nature of the $NO_3\cdot$, its concentration remains very low during the day and increases during the night, the same is true for N_2O_5. As a reservoir of NO_x, these can react with water vapour resulting in wet deposition of NO_2.

When NO_2 is present in large quantities in the troposphere, it reacts with hydroxyl radical (OH) to produce nitric acid (HNO_3). This Equation 2.12, represents the primary homogeneous gas-phase sink for NO_x.

$$NO_2 + OH + M \rightarrow HNO_3 \hspace{3cm} \text{Equation 2.12}$$

2.2 Interaction of Molecules with Electromagnetic Radiation

The sun being the main source of energy emits energy in the form of electromagnetic radiation, among others, UV, visible and infrared (IR) radiation reaches the surface of the earth, while shortwave radiation such as x-rays, is absorbed and converted to heat by the planet's protective layers. The received energy interacts with particles in the atmosphere in three forms; absorption, scattering and transmission. Passive DOAS encompasses the
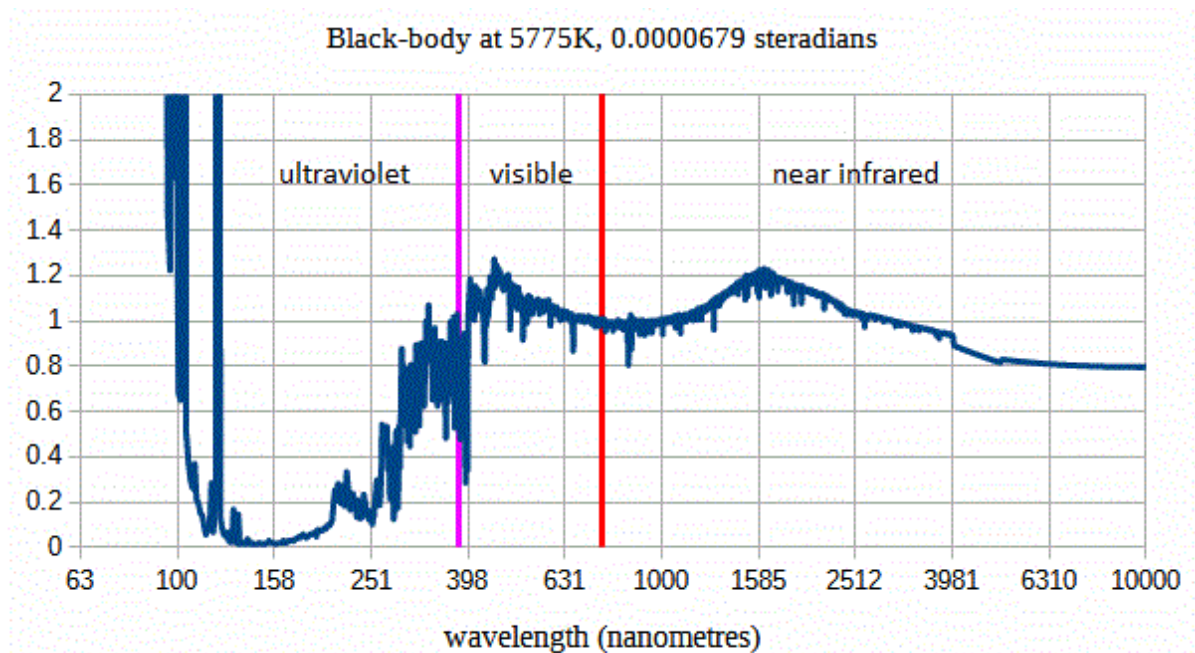
Fig. 2.3: Ratio of solar flux (above atmosphere) to black body flux measured at 5775K. UV range (100-390 nm), visible range (390-750 nm), and infrared range (800-10000 nm), (Wikipedia contributors, 2024).

absorption and scattering (extinction) behaviour of a molecule to study it. This section is limited to the extinction property of trace gases.

A body that absorbs electromagnetic radiation at any angle and frequency is known as a black body. When heated, a black body continuously emits thermal radiation that depends on its temperature, as described by Planck's law (Equation 2.13). The sun, as a Planck emitter, is considered a nearly perfect black body with a surface temperature of approximately 5800 K. It emits a broad spectrum of radiation, with the peak occurring in the visible range, (Goody, 1995).

$$B(\lambda, T) = \frac{2hc^2}{\lambda^5} \cdot \frac{1}{e^{\frac{hc}{\lambda kT}} - 1} \qquad \text{Equation 2.13}$$

Planck's law describes the spectral radiance $B(\lambda, T)$ of electromagnetic radiation as a function of wavelength λ and temperature T emitted by a black body in thermal equilibrium. The speed of light c is a fundamental constant that connects wavelength and frequency, $c = \lambda f$. The Boltzmann constant k relates the average kinetic energy of particles to temperature $\overline{K.E} = \frac{3}{2}kT$, which is measured in Kelvin.

However, when the ratio of this theoretical model and the actual measurements of solar radiation before it reaches the Earth's atmosphere was plotted, as shown in Fig. 2.3, discrepancies arose. The measured solar radiation exhibits significant variability, particularly in the ultraviolet (UV) range below 250 nm, where the two spectra do not align well. This indicates that while the sun approximates a black body in many respects, there are notable differences in its radiation profile.

Interestingly, along the visible and near-infrared region, some absorption bands represented by the deep in the spectrum are found known as Fraunhofer lines. These occur when a specific wavelength of light is absorbed by the sun's atmosphere (chromosphere) leaving a permanent absorption line in the spectrum. The phenomenon discovered by William Hyde Wollaston in 1802 was studied systematically by Joseph von Fraunhofer when he mapped over 570 of these lines in 1814.

2.3 Wavelength Dependency of Absorption

The predominant nature of some trace gas molecules to translate, oscillate, or even vibrate makes them suitable for absorbing electromagnetic radiation. Each molecule has

a unique absorption spectrum which can be used to identify it in remote sensing, Fig. 2.4 illustrates the absorption cross-section of some trace gases as a function of wavelength, O_4 has a single peak around 478 nm whereas, water vapour has two absorption bands in the visible wavelength range, NO_2 has a very pronounced and rapid varying spectrum
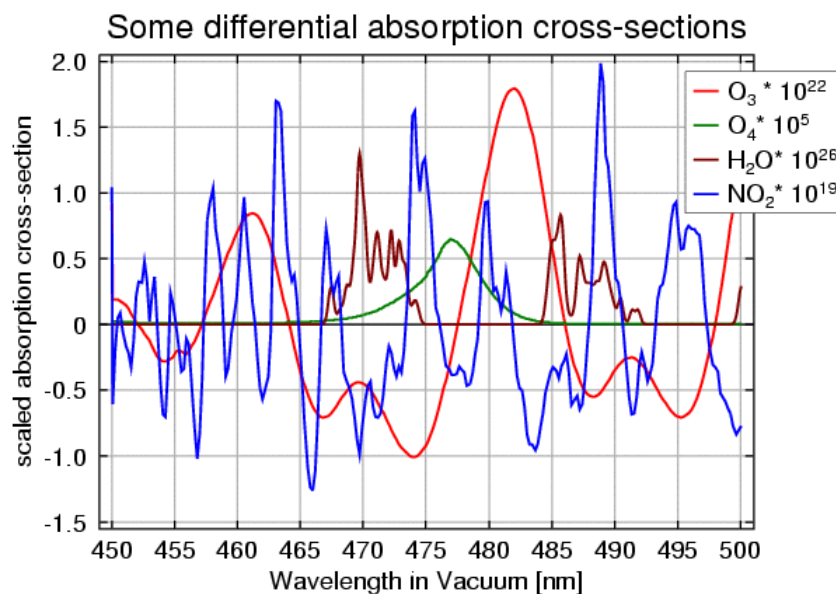
Fig. 2.4: Sample molecular absorption cross-section of ozone
(red line), tetra oxygen(green line), water vapour (brown line)
and nitrogen dioxide (blue line), (IUPB DOAS group, 2024).

compared to the slow and smooth curve of O_3, this demonstrates especially NO_2 suitability in applying DOAS retrieval algorithms discussed in 3.1.

As previously mentioned, molecules in the atmosphere absorb and scatter radiation. The type of scattering depends on the size of the scattering particles relative to the wavelength of the radiation, which can result in either Mie or Rayleigh scattering (elastic scattering) (GERHARDT, 2006).

Another important inelastic scattering process is rotational Raman scattering, where photons change the energy and consequently their wavelengths. This phenomenon is known as the Ring effect, (GRAINGER & J., 1962) and (VOUNTAS, ROZANOV, & BURROWS, 1998). The Ring effect causes a reduction in the intensity and broadening of observed Fraunhofer lines and other absorption features. Specifically, Fraunhofer lines observed at larger solar zenith angles (SZA) appear weaker than those observed at smaller SZAs. This is the angle between the sun's rays and the local zenith. This discrepancy poses a

challenge in the DOAS method, as the atmospheric absorptions being measured are much smaller than the weakened Fraunhofer lines.

3 Methods

During the CINDI-3 Intercomparison exercise, a variety of techniques were employed to enhance the DOAS retrieval method, making it highly versatile for different applications. These techniques included mobile approaches using car-based DOAS and airborne measurements and ground-based and in situ instruments, all operated independently. Notably, these robust instruments utilised DOAS retrieval methods to analyse absorption spectra in the atmosphere and quantify the concentrations of various gases. While this work does not provide a comprehensive overview of all participating instruments, it will highlight the MAX-DOAS system in the following sections, as it operates similarly to the IMPACT instrument.

3.1 DOAS Technique

The foundations of this atmospheric remote sensing technique can be traced back to the 18th century when Pierre Bouguer developed an empirical law relating light extinction to the properties of the medium (σ_A) through which it travels. Building upon this, Johann Heinrich Lambert showed that light intensity loss (dI) is directly proportional to the intensity (I) and path length *s*. August Beer later expanded on Lambert's work, demonstrating that light absorption in a solution is proportional to the sample concentration (ρ_A), (Wikipedia Contributors, 2024).
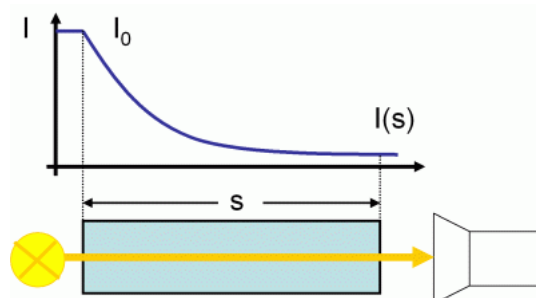
Fig. 3.1: Exponential decrease of light intensity explained based on Lambert Beer's law, (IUPB DOAS group, 2024).

In the early 20th century, the observations of Bouguer and Beer were combined with Lambert's mathematics to formulate the modern Beer-Lambert law, a fundamental relationship in spectroscopy that allows the determination of absorbing species' (i) concentrations from measured absorbance Equation 3.1, (Wikipedia contributors, 2024).

$$dI = -\rho_A \, \sigma_A \, I \, ds \qquad \text{Equation 3.1}$$

$$I(s) = I_0 \exp\{-\sigma_A \, \rho_A \, s\} \qquad \text{Equation 3.2}$$

Integrating the differential form of Equation 3.1 leads to an exponential function of the initial light intensity as seen by the blue curve of Fig. 3.1. Equation 3.2 is based on the assumption of a homogeneous medium that only involves absorption processes. However, this assumption does not apply to the atmosphere. In reality, the atmosphere contains various gases, each with distinct absorption characteristics. As a result, the overall light attenuation is influenced by the combined effects of these different N gases, leading to a more complex interaction than Equation 3.2 suggests.

As pointed out before, in addition to absorption processes scattering also plays a significant role. Mie scattering which has a wavelength dependency of $\sigma_{Mie} \sim \lambda^{-1.5}$ and Rayleigh scattering which follows $\sigma_{Ray} \sim \lambda^{-4}$. To accurately account for the effects of Rayleigh and Mie scattering, Equation 3.2 needs to be adjusted by subtracting their contributions. This requires Equation 3.1 to be rewritten specifically for Rayleigh and Mie scattering. By doing this, the wavelength (λ) dependencies of these scattering processes can be incorporated, leading to the formulation in Equation 3.3.

$$I(s,\lambda) = I_0(\lambda)\exp\left\{-\sum_{i=1}^{N}\sigma_{A_i}(\lambda)\rho_{A_i}s - \sigma_{Ray}(\lambda)\,\rho_{Ray}\,s - \sigma_{Mie}(\lambda)\,\rho_{Mie}\,s\right\} \quad \text{Equation 3.3}$$

The temperature profile as a function of altitude, alongside atmospheric inhomogeneity, causes the concentration of absorbers to vary along the light path. This variation necessitates the introduction of the concept of slant column (SC) as shown in Equation 3.4, which represents the integral of absorber concentration from the ground to the top of the atmosphere. This variability presents challenges, especially when the light path changes, such as when observations are not made directly toward the sun.

$$SC_i = \int_0^{TOA} \rho_{A_i} ds \qquad \text{Equation 3.4}$$

Substituting for Equation 3.4 in Equation 3.3 gives

$$I(s,\lambda) = I_0(\lambda)\exp\left\{-\sum_{i=1}^{N}\sigma_{A_i}(\lambda)SC_i - \sigma_{Ray}(\lambda)SC_{Ray} - \sigma_{Mie}(\lambda)\,SC_{Mie}\right\} \quad \text{Equation 3.5}$$

The total spectral attenuation is divided into a high-frequency part related to the trace gases pronounced, rapidly varying molecular absorptions and a low-frequency part accounting for elastic scattering on molecules, aerosols, clouds, and instrumental throughput. This methodology is what led to the term "differential" in DOAS. Taking the polynomial order of the scattering effects (j), a simple approximation can be introduced to take care of processes other than absorption as shown in Equation 3.6. Inelastic scattering effects, such as the Ring effect are considered using a pseudo-cross-section (Peters, et al., 2019).

$$I(s, \lambda) = I_0(\lambda)\exp\left\{-\sum_{i=1}^{N}\sigma_{A_i}(\lambda)SC_i - \sum_{j=0}^{M}p_j\lambda^j\right\} \qquad \text{Equation 3.6}$$

Taking the natural logarithm of Equation 3.6 and moving the initial intensity to the left-hand side gives Equation 3.7 known as the DOAS equation.

$$\ln\frac{I(\lambda)}{I_0(\lambda)} = -\sum_{i=1}^{N}\sigma_{A_i}(\lambda)\,SC_i + \sum_{j=0}^{M}p_j\lambda^j \qquad \text{Equation 3.7}$$

The DOAS equation includes several unknowns, specifically $N+M+1$ variables that need to be determined, along with measurable quantities I and I_0. While it may seem impossible to solve an equation with multiple unknowns, the advantage lies in the fact that the equation is applicable at each wavelength. Each wavelength provides unique information and distinct absorber cross-sections. This characteristic allows for using standard linear least squares fitting to determine the slant column and the polynomial terms effectively.

3.2 Light Path

From a measurement perspective, Lambert-Beer's law indicates that the attenuation of light depends on its intensity, this is a function of the light path, the route taken by photons through the atmosphere before being collected by the instrument. Two modes of this collection will be discussed in the following section.

3.2.1 Zenith-Sky Measurement

With an instrument positioned to look vertically up to the sky, radiation scattered above the instrument are collected. This, in particular, is relevant for stratospheric absorbers (example O_3), the length of the light path changes with a change in the solar position.

Measurements at larger SZA have longer stratospheric light path compared to noon measurements, however the shorter light path through the troposphere remains rather unchanged as shown in Fig. 3.2.
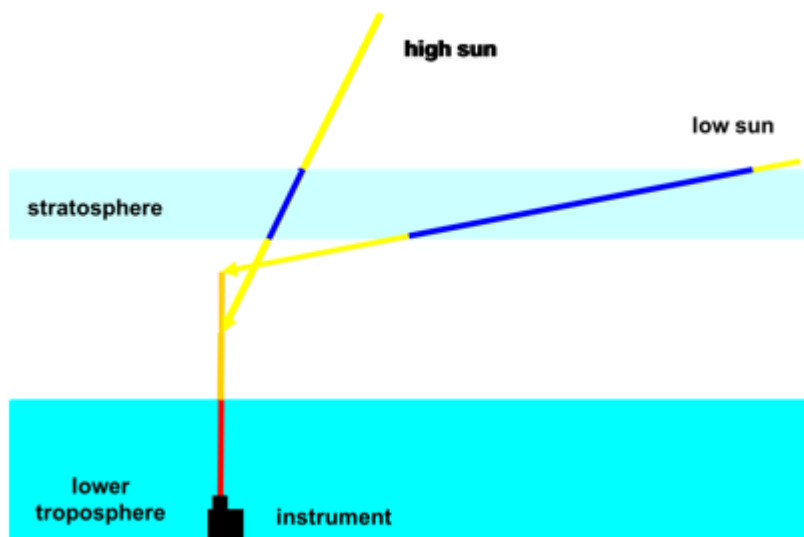
Fig. 3.2: Zenith-sky geometry, (IUPB DOAS group, 2024).

3.2.2 Off-axis Measurement

Any observation between the horizon (0°) and the zenith-sky (90°) is classified as an off-axis measurement. The viewing direction referenced from the ground to the instrument is known as the elevation angle(θ). Like the zenith-sky, off-axis measurements provides an identical stratospheric light path across varying elevation angles. Lower elevation
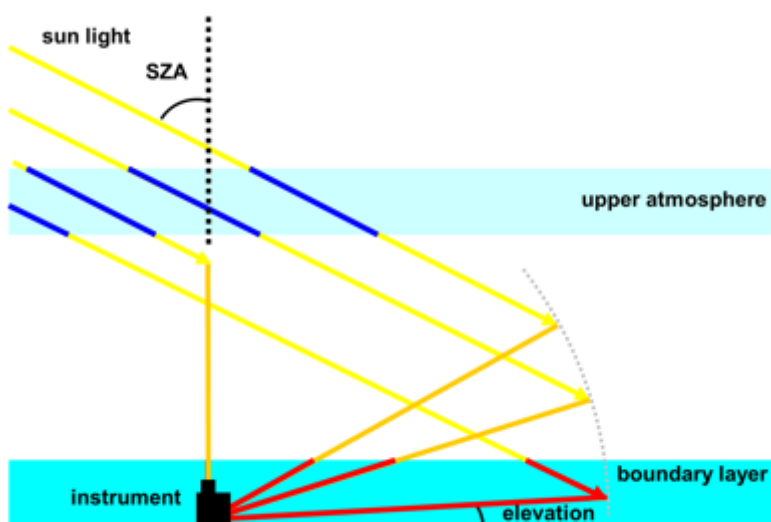
Fig. 3.3: Off-axis geometry, (IUPB DOAS group, 2024).

angles result in longer light paths through the troposphere, while they decrease with higher elevation angles (see Fig. 3.3). This characteristic makes lower elevation angles particularly effective for measuring tropospheric absorbers like NO_2. Consequently, the sensitivity of off-axis measurements depends on the selection of the elevation angle, which minimises solar position dependency.

To solve the DOAS equation, two sets of measurements are required. However, since I_0 cannot be obtained in the presence of absorbers, we can replace I_0 by taking measurements along different light paths and calculating their difference which yields a differential slant column. In this context, the shortest light path serves as a background reference: for zenith-sky measurements, this is represented by high solar angles, while for off-axis measurements, it corresponds to the zenith direction where the tropospheric light path is shortest.

3.3 Vertical Column

The introduction of Equation 3.4 was prompted by the variation in absorber concentration throughout the atmosphere. However, the slant column is highly dependent on the length of the atmospheric light path, which can complicate the interpretation of measurements under different atmospheric conditions, such as the presence of aerosols and clouds, and it is often unclear how many scattering events occur in the atmosphere. In contrast, the vertical column (VC) is independent of the light path, it represents the integral of absorber concentration along the vertical axis from the surface to the top of the atmosphere. The VC provides the total concentration of gas along this vertical axis, as Illustrated in Fig. 3.4. The ratio between SC and VC is defined as air mass factor (AMF).

$$AMF_{strat.} \equiv \frac{SC_\phi}{VC} \cong \frac{1}{cos(\phi)} \qquad \text{Equation 3.8}$$

$$AMF_{trop.} \equiv \frac{SC_\theta}{VC} \cong \frac{1}{sin(\theta)} \qquad \text{Equation 3.9}$$

The air mass factor (AMF) can serve as a useful tool for computing the length of the light path, but its calculation can be complex. In zenith-sky measurements, a simple geometric approximation can be applied using the SZA (ϕ), as given by Equation 3.8. However, as the SZA reaches 80°, this approximation becomes invalid because scattering limits the possible path length, and the spherical nature of the atmosphere no longer allows for longer light paths at this angle.
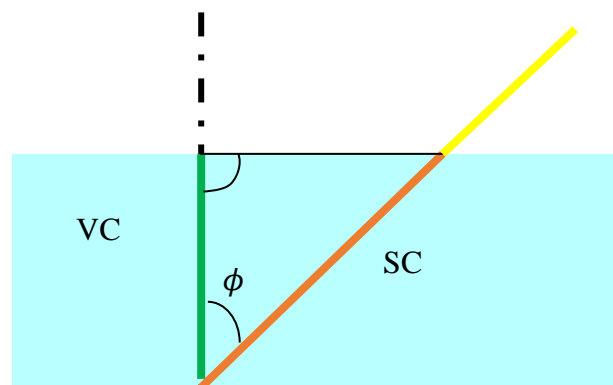
Fig. 3.4: Vertical column geometry. (IUPB DOAS group, 2024).

For off-axis measurements, the approximation holds for larger elevation angles (θ), as shown in Equation 3.9. The question arises: how precise can this approximation be? It turns out that this approximation holds true only when the most probable scattering point is above the absorbing layer. This situation occurs, for example, during high noon for zenith-sky measurements and at higher elevation angles for off-axis measurements.

Since the AMF depends on the wavelength and the vertical distribution of the absorber, a complex system of equations that includes radiative transfer models is used to solve for the light path, this complexity is beyond the scope of this work. As a result, this study will focus on using differential slant column densities (DSCD).

3.4 Slant Column

Based on the principles outlined in earlier sections, the slant column densities of gases are measured and analysed using a computer-based software system developed by the IUP Bremen DOAS working group. The process starts from the data acquisition down to the computation of vertical column files, which ensues several steps each accounting for a particular output parameter, this ensures enough flexibility in managing the data and creating a smooth data analysis procedure.
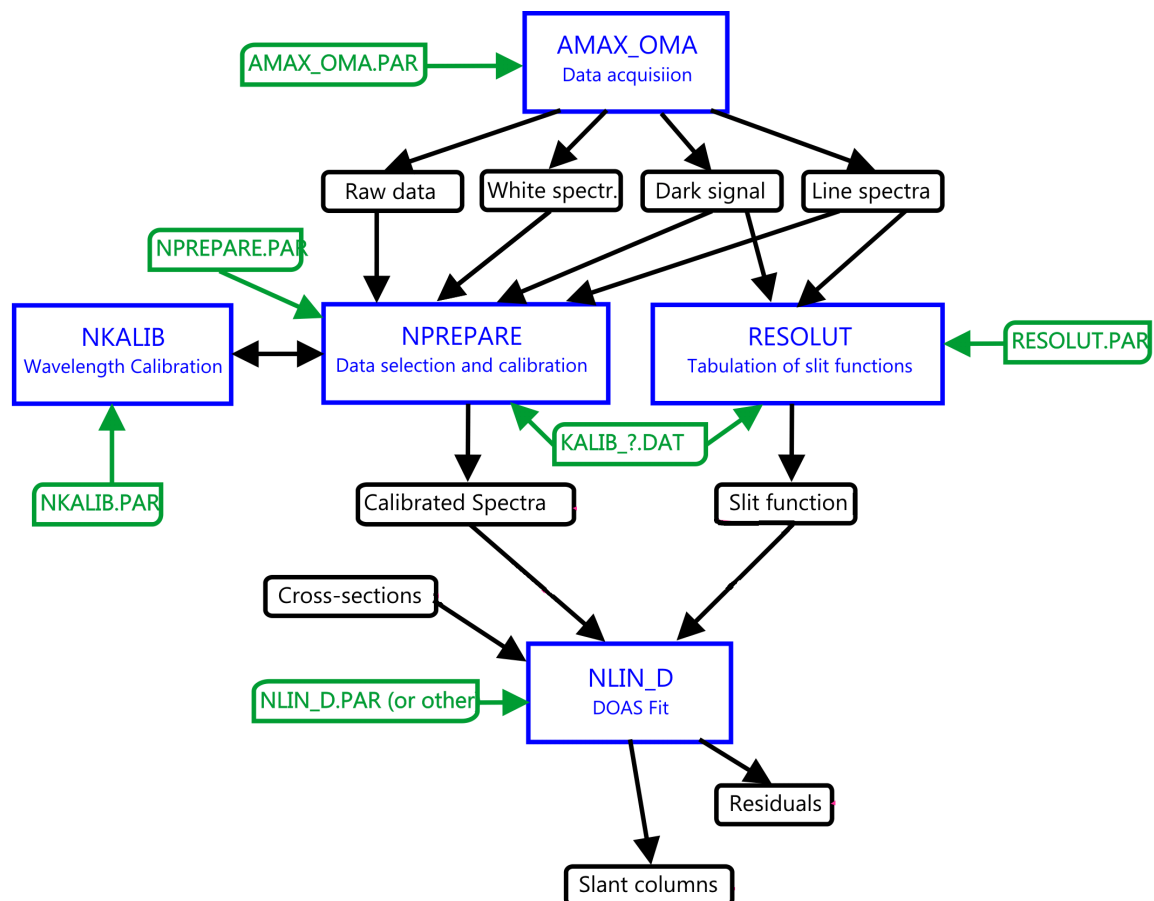
Fig. 3.5: Schematic of the data evaluation of ground-based DOAS measurements, (Richter, 2024).

The DOAS step-by-step fitting procedure is described in Fig. 3.5, the blue boxes represent executable software packages that take defined functions from parameter files (shown in blue) and produce datasets (shown in black) as output files in the DOAS retrieval process. While this encompasses the general steps for any ground-based DOAS instruments, the measurement processes used by IMPACT are no different. Specific functions of the programs can be found in (Ostendorf, 2017).

3.5 IMPACT Characterisation

Similar to other DOAS instruments, IMPACT is an optical remote sensing device that operates through a combination of software and hardware systems. Detailed information on its development and initial deployment, can be found in the comprehensive study conducted by (Ostendorf, 2017). This section will not only outline the working principles of IMPACT but also discuss the testing and optimisation processes undertaken to enhance the instrument's performance.

Sunlight scattered in the atmosphere is collected by a telescope from various viewing directions. This light is then separated by wavelength using a spectrometer and subsequently read out with a charge-coupled device (CCD). IMPACT employs imaging methodologies to ensure large vertical coverage and 360° azimuthal pointing for a high-resolution retrieval of atmospheric gases. The integration of DOAS and imaging

Fig. 3.6: Outdoor parts of IMPACT.

capabilities allows for the detection of temporal variations of atmospheric trace gas conditions, making it a vital tool in precise atmospheric research.

3.5.1 Components

The telescope of the IMPACT instrument Fig. 3.6 mounted on a tripod features a pan-tilt head comprising of a mechanical motor which controls the axial movement in both horizontal and vertical orientation. This allows for the azimuthal and elevation control.

The indoor components of the instrument Fig. 3.7 comprise an imaging spectrometer of the Czerny–Turner type which uses a 68 by 68 nm grating size to separate visible light in to different spectral lines according to wavelengths, equipped with a CCD camera which receives the spectrally splitted light and stores it as counts on a pixel.

A computer receives the data through a software program and stores the measurements to disc for further analysis. The working temperature (Usually +35 degrees Celsius) of the spectrometer is regulated by evenly distributed heating foils regulated by a temperature controller to prevent thermal and spectral drifts. The indoor and outdoor components

are linked by a bundle of vertically superimposed fibres, the pan-tilt cable and a video cable.

Fig. 3.8 shows the assembled scheme of IMPACT. The main working components in black boxes are inter-connected by data cables, power cables via adapters all powered by an uninterrupted power supply (UPS) that allows for quick data saving and backups during power outage.
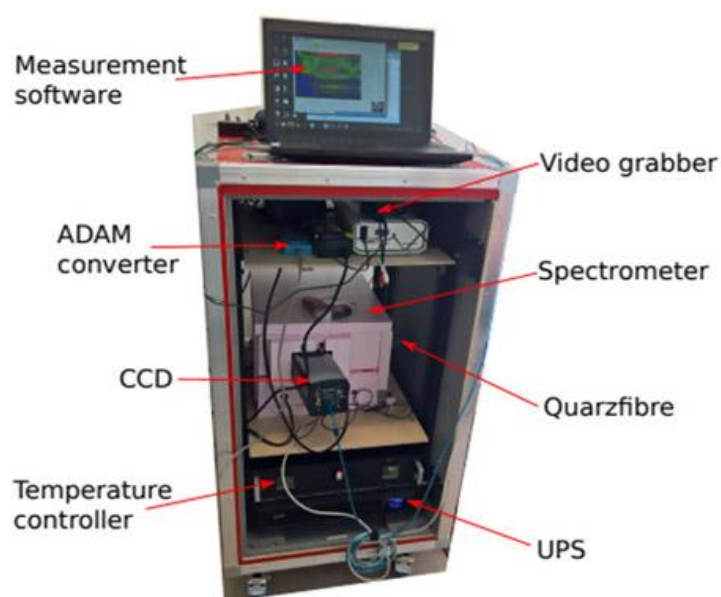
Fig. 3.7: Indoor parts of IMPACT, (Ostendorf, 2017).
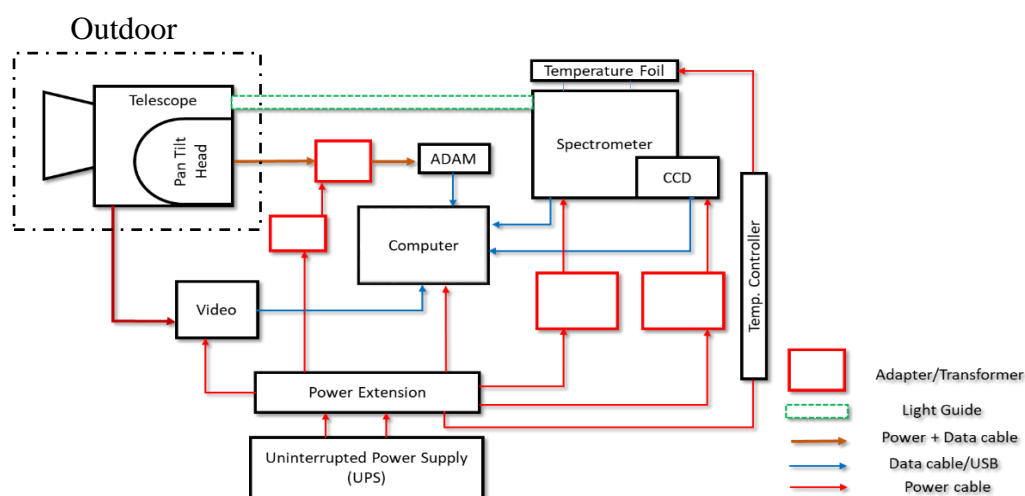
Fig. 3.8: Scheme of IMPACT Instrument.

Table 3.1: IMPACT technical documentation.

IMPACT Component	Specification	
Telescope	Mount	C-Mount
	Focal length [mm]	8 mm
	Angle of view	D: 67.1°, H: 56.3°, V: 43.7°
	Temperature	-10℃ - 50℃
Light guide	Type	Non-Circular Core
	Number of optics	50
	Width	0.123 mm
	Active light area	0.01 mm^2
Spectrometer	Type	Andor Shamrock SR303i-A
	Spectral window	420 – 460nm
	Wavelength resolution	0.1nm
	Focal length	303 mm
	Aperture	f/4
	Size	394 x 238 x 208 mm
	Weight	20 kg
	Grating size	68 x 68 nm
Coupled charged device	Type	Andor Newton DU940P-BU
	Active pixels	2048 x 512
	Pixel size	13.5 x 13.5 µm
	Image area [mm]	27.6 x 6.9 mm
	Digitisation	16 Bit
	Max air-cooled	-80℃
	Linearity	Better than 99%
Pan and tilt head	Type	ENEO VPT-501
	Elevation	±90°
	Azimuth	±180°
	Rating	24 VAC - 120 W
ADAM converter	Type	ADAM-4520
	Interface	RS-232/-485
	Baud rate (bps)	1200 - 115200

	Power supply	24 V$_{DC}$
	Type	APC smart-ups C 1000
	Battery capacity	10000 VA
Uninterrupted power supply	Weight	20.5 kg
	Temperature	0°C to 40°C
	Output voltage	120 VAC

Table 3.1 shows a summarised technical documentation of the main components of IMPACT, although many of the parts were according to the manufacturer's design, however, some level of prescription was given to the manufacturer before the production of some parts e.g. the light guide.

3.5.2 Imaging Optimisation

The light displayed by the CCD chip takes a compromise approach. The method explained by (Ostendorf, 2017) optimises both spectral lines and image quality. The IMPACT CCD has 512 by 2048 pixels, since the imaging does not necessarily require a full frame of the CCD chip, 285 vertical pixel columns were left cutting out the broadening observed along the y-axis. The topmost part of the chip serves as a registry where information of every pixel row on the CCD is read, each row is shifted to the register vertically (see Fig. 3.9) which makes all but one collect more signal from other rows when chip is still illuminated.
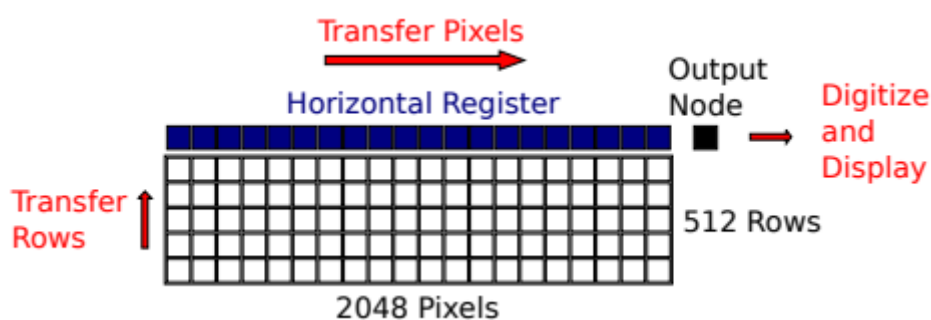
Fig. 3.9: CCD Read out mechanism, (Ostendorf, 2017).

This can corrected in two ways; using a shutter during readout which is rarely used due to low efficiency of the shutter or by smear correction technique. In this technique, the falsely acquired light is corrected by estimating the time of the readout and accounting

for the amount of light collected during this time, this increases sequentially as the smear of a third row would be the sum of the first and second. However, the correction has its problem as it is not watertight and affects mostly the lower part of the chip containing the information of lower elevations close to the boundary layer, therefore, the light fibre from the telescope is flipped to allow the lower elevations to be read out first.

Having the light guide orientation flipped for the first time suggested some alignment issues with its stopper as shown in Fig. 3.10, However, this was followed up with some testing for the evaluation of the effect which later showed no harm to the focus of the objective lens.

a)   b)
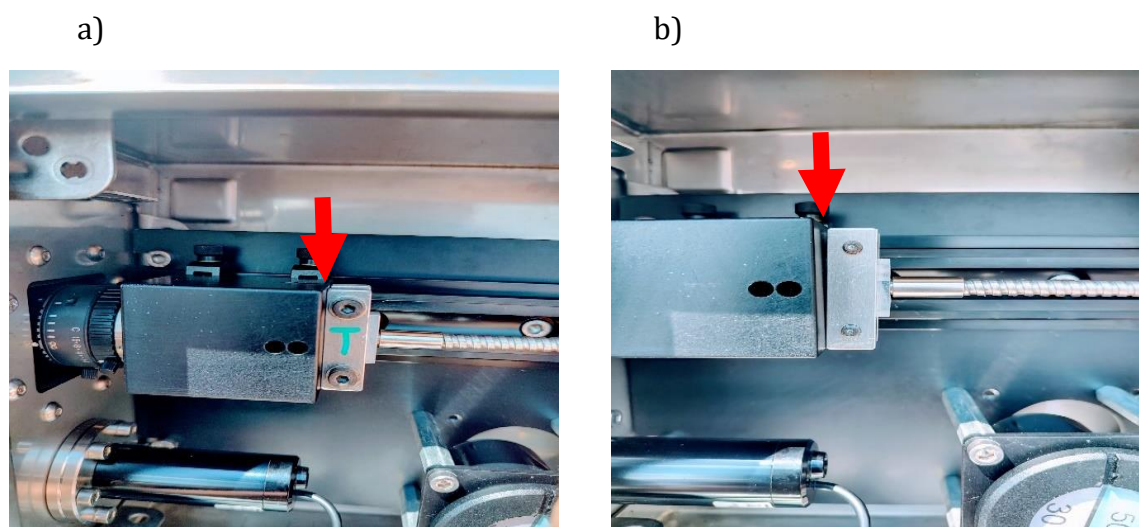
Fig. 3.10: Light guide alignment in the telescope before (a) and after (b) flipping.

3.5.3 Saturation Control

Signal intensity on a CCD has a linear correlation with the acquisition time, at longer exposure time and under a sunny atmosphere, the CCD tends reaching saturation level where data cannot be used.

To correct for that, a test is needed to determine how long before the instrument's
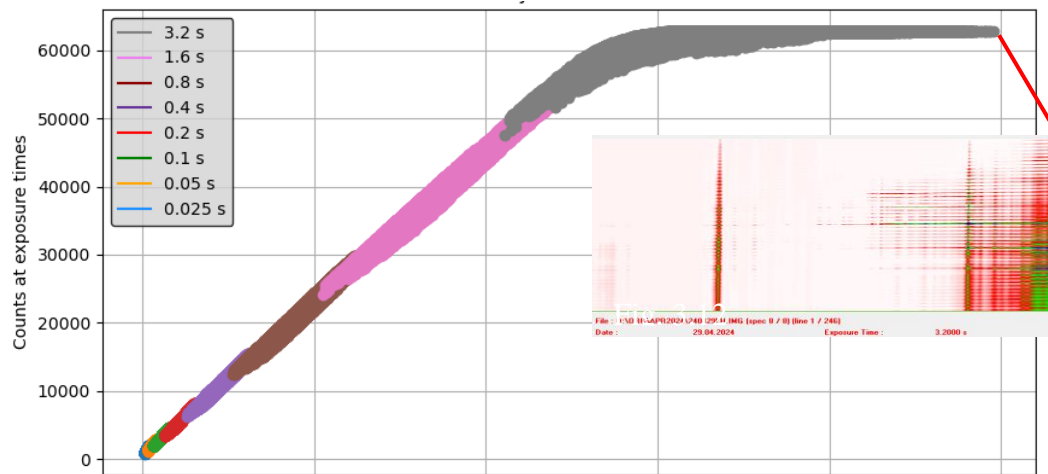
Fig. 3.11: IMPACT Linearity function, spectral image at 3.2 s exposure time (attached box).

linearity breaks, in that case a neutral density filter can be installed to regulate the amount of light entering the window thereby extending the saturation time of the instrument. A software automated measurement of sunlight on a clear sunny atmosphere was conducted in Bremen at different exposure times, from 0.025 s to 3.2 in multiples of 2 controlled by a mechanical shutter. This allows for the observation of non-linearity especially at smaller exposure times.

Fig. 3.11 shows the intensity count as a function of the expected intensity as exposure time increases. The plot illustrates that the instrument reaches saturation (as indicated by the attached image) after 1.6 seconds of exposure time. Additionally, the instrument loses its linearity at counts exceeding 50,000, resulting in the need to discard any data above this threshold. After correcting for the noise caused by an estimated shutter delay of 0.031 s, Fig. 3.12 illustrates a good linearity agreement even at smaller time steps until the IMPACT saturation at 60000 counts.
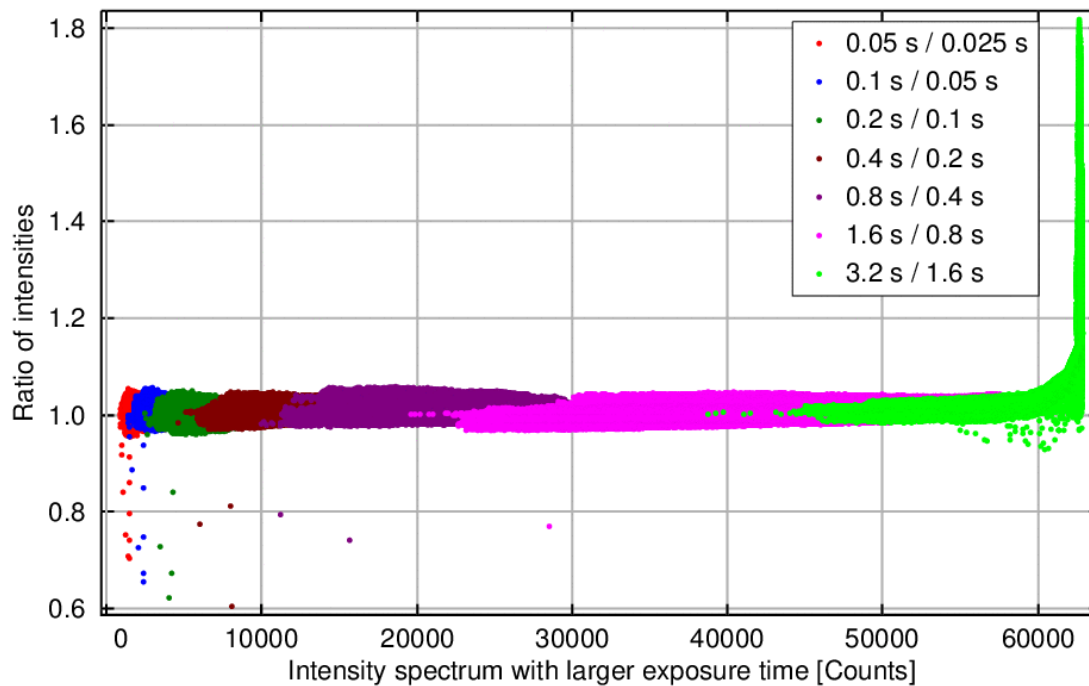
Fig. 3.12: Intensity ratio of linearity response with shutter delay correction.

4   The Cindi-3 Campaign

Research activities aimed at enhancing measurement techniques and broadening application ranges necessitate the ongoing development and operation of a diverse array of instrumental designs. This demand has led to the establishment of regular intercomparison campaigns, including the *third* **C**abauw **I**ntercomparison campaign of **N**itrogen **D**ioxide measuring **I**nstruments (**CINDI**-*3*), which is the focus of this study.

Succeeding by CINDI of 2009, the CINDI-2 campaign held in 2016 provides a conclusion and recommendations for improving and standardising UV-visible MAX-DOAS measurements of several key atmospheric trace gases like; NO_2, HCHO and O_3. In line with its aim of better understanding the measurement technique and data evaluation approaches, The CINDI-3 targeted characterising the level of consistency between UV-Vis DOAS instruments operated worldwide and used for satellite validation and science investigations on atmospheric composition variability and trends (CINDI-3 Coordination Team, 2024).
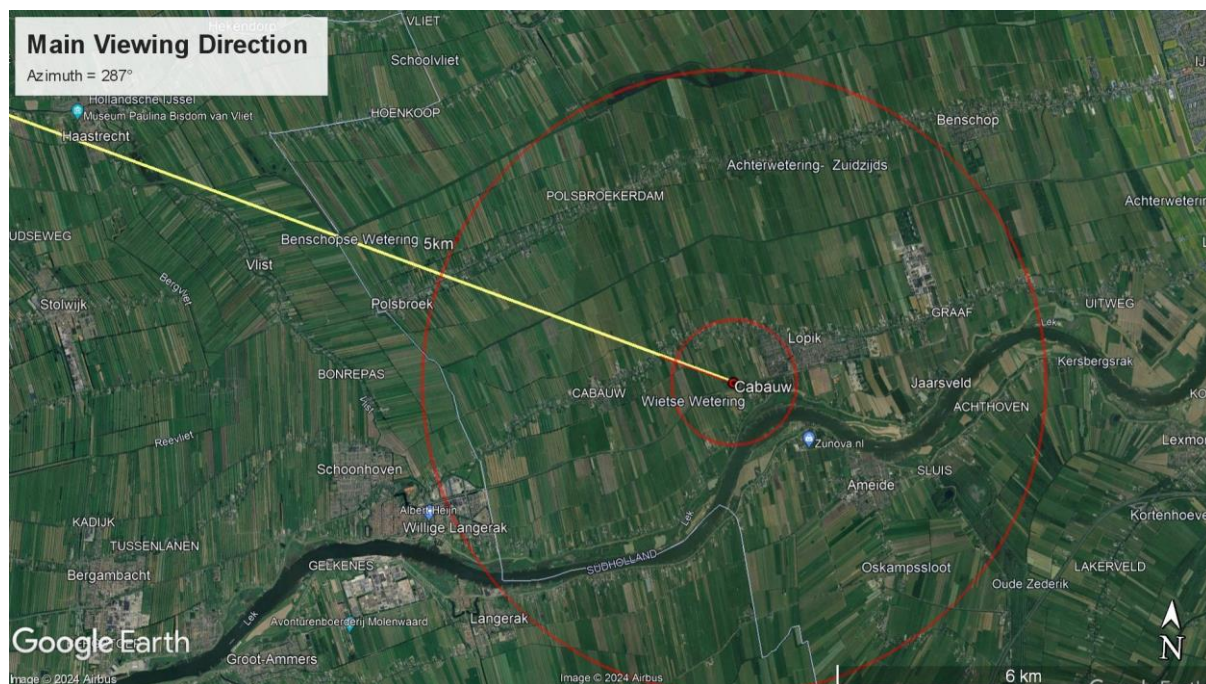
Fig. 4.1: Google earth view of CINDI-3 site location showing main viewing direction at the CESAR Remote-Sensing Site (RSS).

The CINDI-3 campaign which took place at CESAR remote-sensing site located at 51.96800 ° N, 4.92900 ° E (Fig. 4.1) was supported by top-level European institutions such as the European Space Agency (ESA) which is particularly interested in satellite validation and scientific investigation, the Network for the Detection of Atmospheric

Composition Changes (NDACC) which evaluates the consistency of instruments, Fiducial Reference Measurements for Ground-Based DOAS Air-Quality Observations (FRM4DOAS) providing centralised data processing system which provides a service for MAX-DOAS data processing within the pan-European ACTRIS (Aerosol, Clouds and Trace Gases Research Infrastructure) research infrastructure and individual research groups across the globe for joining the interface of global reference network of atmospheric science.

4.1 Protocols

The five-week intercomparison campaign began on May 21, 2024, with one week dedicated to instrument installation, testing, and various calibration activities. The three weeks of intensive measurements followed, including periods of semi-blind intercomparison hosted by The Royal Netherlands Meteorological Institute (KNMI). The data acquisition schedule for all the participants is strictly defined Fig. 4.2
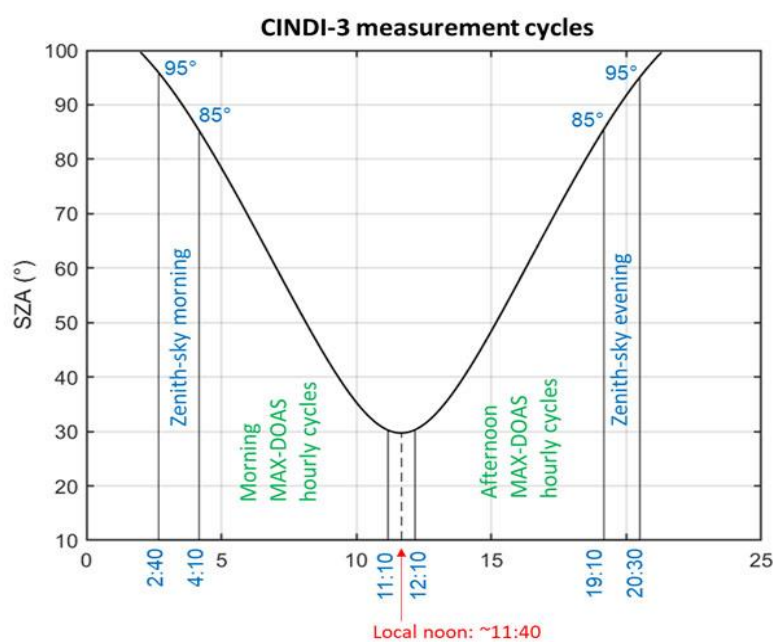
Fig. 4.2: Mean diurnal variation of the SZA at Cabauw during the from May 21 to June 21 over time in UTC. (CINDI-3 Coordination Team,

The key protocols adopted in the exercise include:

a) To ensure precise coordination of the timing and geometry for each individual measurement, allowing all instruments to measure the same air mass.

b) For each data product, a specific set of retrieval settings and parameters is required.

    c) All slant column datasets measured are submitted to an independent campaign referee by the following morning. During daily meetings in the afternoon, the comparison results of the slant columns from the previous day are presented anonymously.

4.2 Set-up

Instruments were installed on top of the site structure made out of two superposed rows of containers with platform height of 6.82 m above water level. The main viewing direction was chosen from high resolution horizon scan as the lowest ground near the measurement site. The campaign schedule containing measurement sequence and hourly routine for every day was introduced to the instruments which they operated based on.

4.2.1 Acquisition Protocol

The reference azimuth direction for comparison is set at 287° north, corresponding to the west-northwest direction. In this convention, 0° represents North and increases clockwise. Based on the geometry of the solar position Fig. 4.2, the daytime period was designated from 4:10 UTC to 19:10 UTC. Within this timeframe, eight hourly cycles, Fig. 4.4 were defined in the morning in the afternoon including a 10 minutes of free sequence. Noon cycle starts at 11:10 to 12:10, Fig. 4.5 was also included and for zenith-sky measurement, data acquisition will occur for one minute at a time throughout the entire day, from 04:40:00 UTC to 19:09:59 UTC.
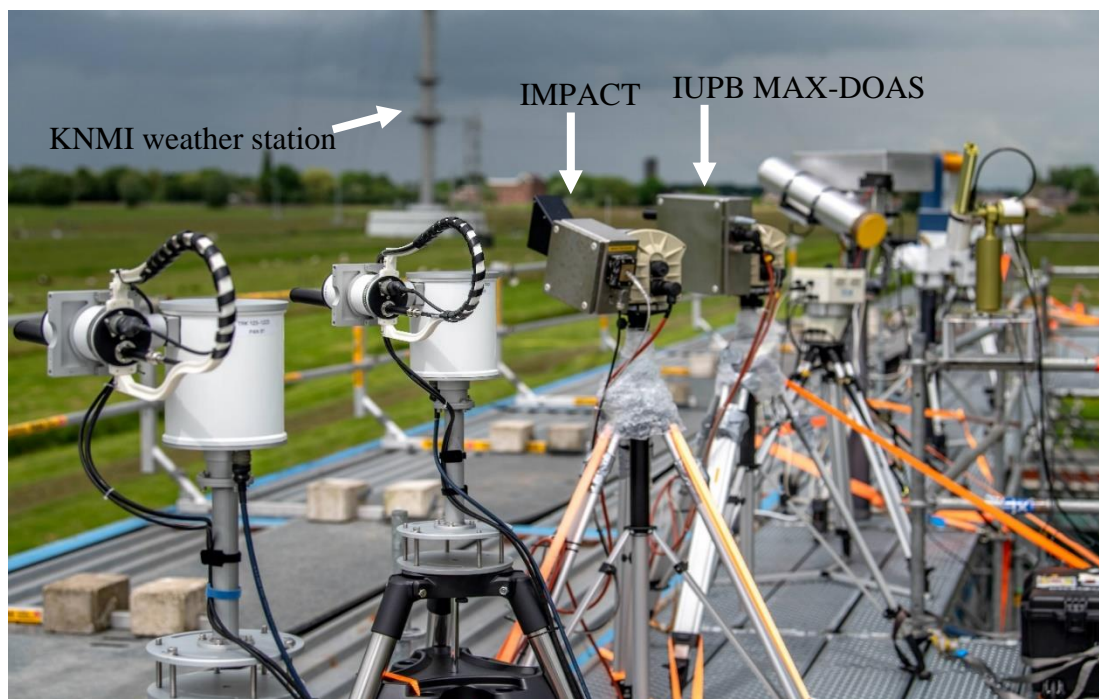
Fig. 4.3: Instruments on containers roof according to KNMI installation order.

IMPACT performance as an imaging DOAS instrument during the CINDI-3 Campaign, 2024

MAX-DOAS hourly cycle
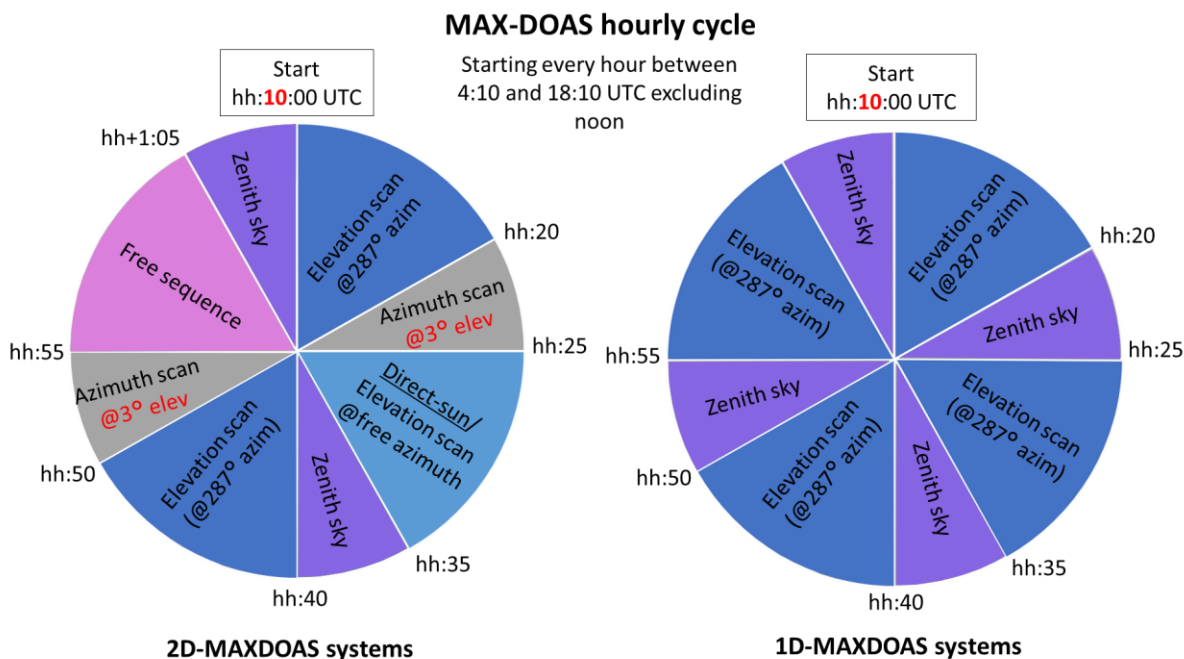
Fig. 4.4: CINDI-3 data acquisition hourly cycles, (CINDI-3 Coordination Team, 2024).

MAX-DOAS noon cycle
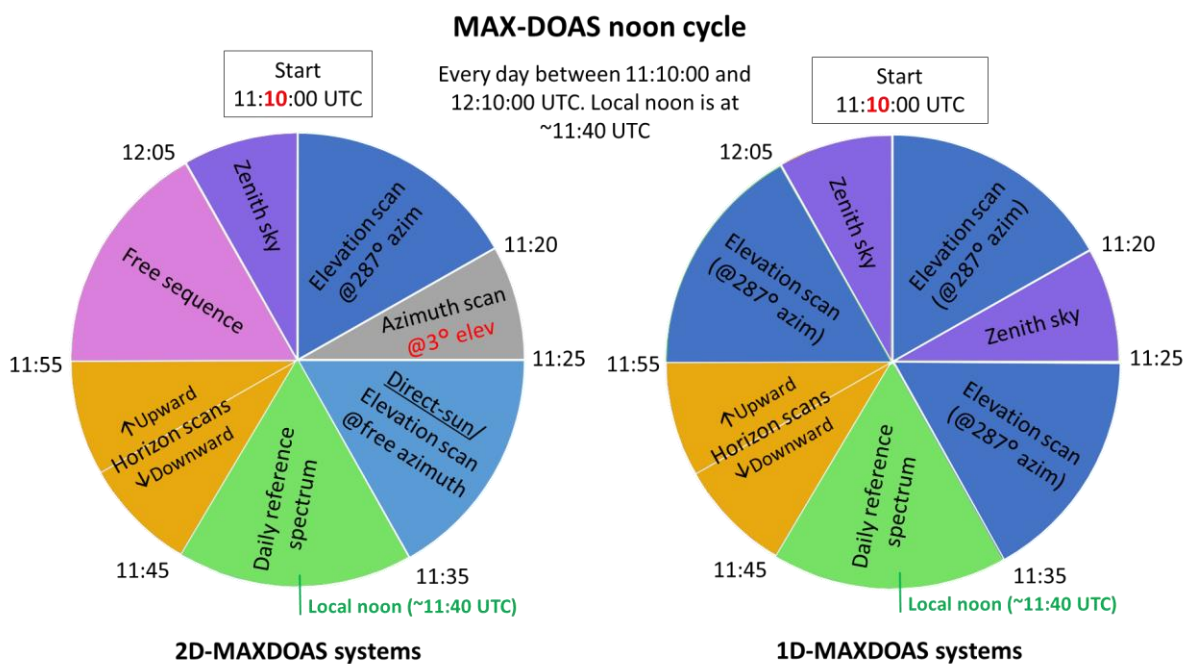
Fig. 4.5: CINDI-3 data acquisition noon cycle, (CINDI-3 Coordination Team, 2024).

4.3 Calibration

To illustrate the concept of calibration, consider the process of measuring the mass of an object using a balance scale. This measurement is only possible when a known mass is placed alongside the unknown mass, only then can the result be determined relative to

the known mass. This principle applies to any type of measurement. Similarly, like other optical remote sensing instruments, IMPACT employs several types of calibrations, which can be broadly categorised into:

    a. Noise calibration

    b. Geometric calibration

    c. Spectral calibration

4.3.1   Noise

With the IMPACT shutter closed and free from illumination, the CCD recorded some relatively constant signals for different measurements. Each pixel has a unique contribution to the overall CCD noise, the noise is generally composed of a constant offset and a signal which linearly depends on the exposure time often called dark current. The signals are mainly electrical and contain both positive and negative values which the CCD cannot read effectively, this is compensated by including the constant offset to avoid biasing the mean of the signal. Fig. 4.6 displays the average dark measurement plotted against exposure time together with the mean deviation (red bars), defined in increments multiples of 2. This specific configuration causes the signal intensity to increase following
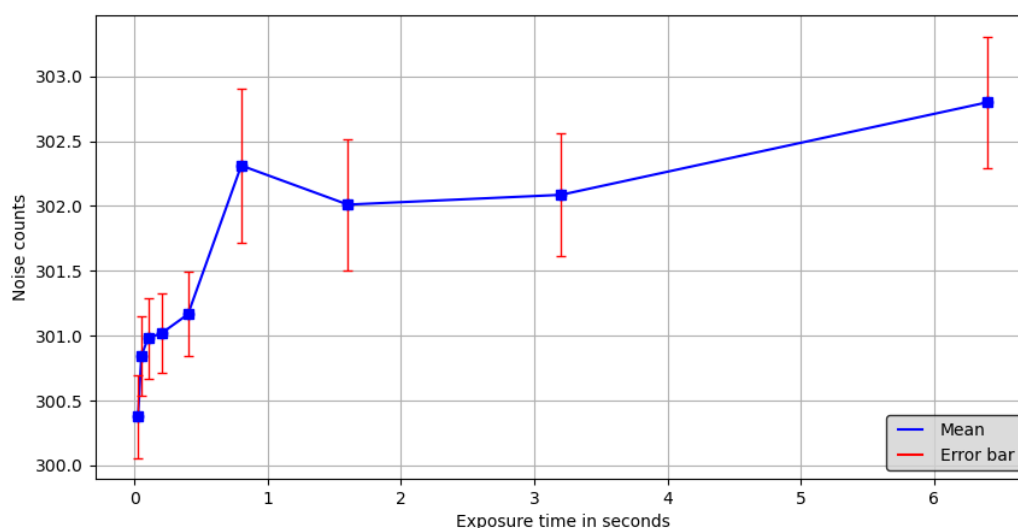
Fig. 4.6: Mean of dark signal.

a logarithmic function. However, longer exposure times do not significantly alter the recorded signal intensity, allowing for more table noise across varying exposure time. The mean deviation was used to understand the dependency of the signal on exposure times. The nearly straight line curve of Fig. 4.7, shows very low dependency on exposure

time. However, the prominent step between lower and higher exposure times divides the trend into two distinct parts, indicating that most of the dark signal arises from the introduced offset.

Prior to the first zenith-sky sequence of each day, i.e. starting at 04:00:00 UTC, the instrument records a set of dark current measurements covering the full range of
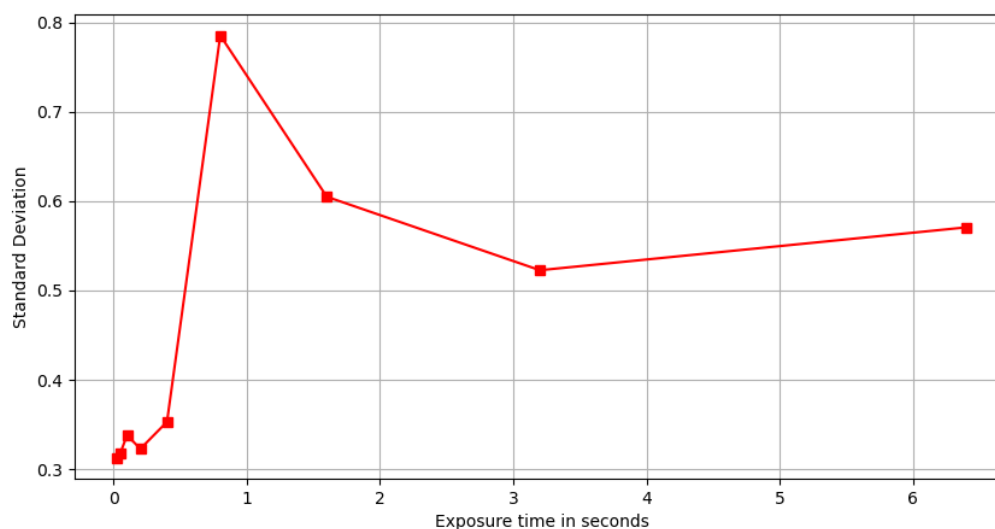
Fig. 4.7: Standard Deviation of dark signal.

exposure times used during the day, this is necessary as the thermal stability of the instrument varies with the temperature fluctuations of the environment.

4.3.2   Azimuthal Calibration

A high-resolution azimuthal scan was used to calibrate the azimuthal direction. This is done by moving the telescope in steps of 0.1° such that the KNMI mast is within the instrument's field of view. The azimuth at which the mast was located (see Fig. 4.8) was

263.7°
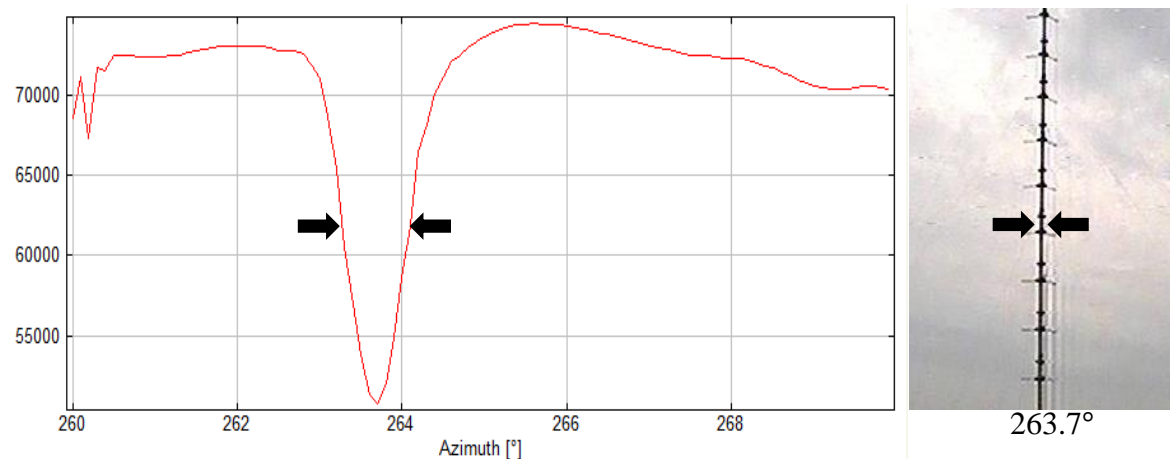
Fig. 4.8: Skyline Scan of KNMI-mast showing signal intensity (y-axis) along azimuth(x-axis).

corrected using the precise GPS coordinates of the mast and the instrument. The primary viewing direction was adjusted based on an offset calculation relative to the mast's azimuth of 263.7°.

4.3.3 Far Lamp Calibration

One of the approaches employed towards the calibration of the instrument's field of view was the far lamp measurement. A car lamp was set up at night at a distance of 1.3 km to the instrument as illustrated in Fig. 4.9 (a), the azimuth of the lamp, measured at 286.8°, was determined by identifying the maximum light intensity emitted from the lamp through a skyline scan, as described in the previous section. After locating the maximum intensity, the elevation angle of the telescope was increased until the lamp was no longer within the FOV. This adjustment was then reversed in increments of 0.2° downward.

(a) Experimental set up for the calibration measurement

(b) Image of the lamp moving across the fibres
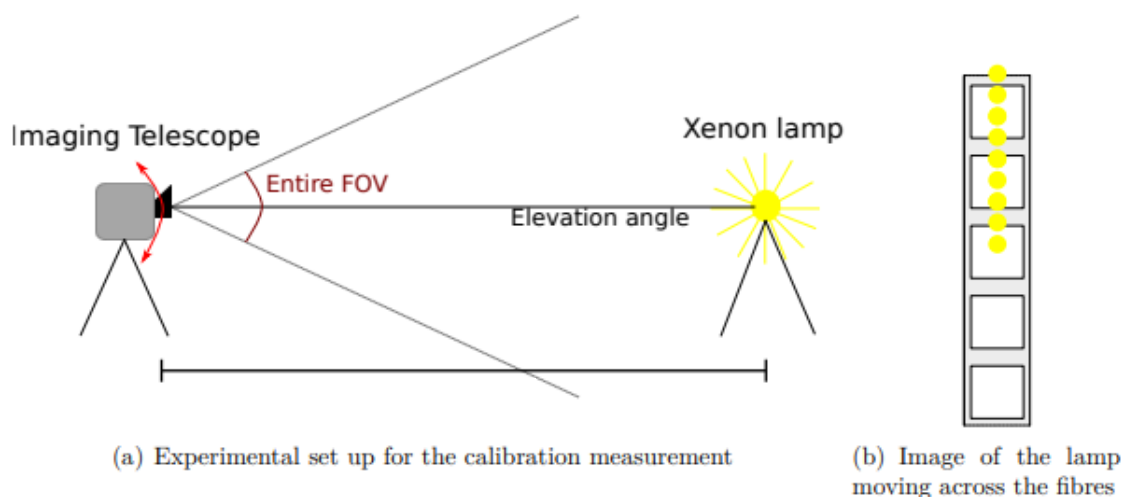
Fig. 4.9: Illustration of far lamp calibration, (Ostendorf, 2017).

The elevation angle shifted the lamp's image across the fibre entrances in the telescope, the imaging of individual fibres on the CCD is independent of the telescope's elevation. For each measurement, only one individual fibre was illuminated, resulting in the lamp's spot at the light fibre entrance being smaller than a single fibre's diameter as illustrated in Fig. 4.9 (b). Additionally, each fibre was illuminated for approximately four steps before the signal switched to the neighbouring fibre in the subsequent measurement. This instantaneous FOV for single fibres was approximately 0.8°, and the intensity of each CCD row was displayed as a function of the telescope's elevation angle

4.3.4 Line of Sight

The elevation angles was determined by binning neighbouring lines on the CCD. Each fibre corresponds to a few lines on the CCD, but adjacent fibres may share intensity. Lines with approximately equal intensity are binned together and assigned to a single stripe, each representing a specific elevation angle. This method allowed to identify which fibre is observing which elevation angle under a specific setup. Fig. 4.10 illustrates a horizon calibration method that was employed to determine the elevation angles based on the
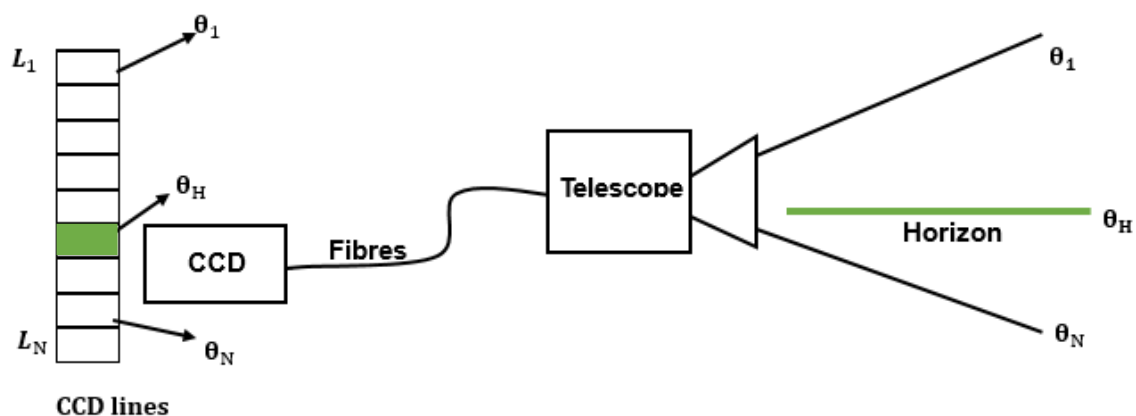
Fig. 4.10: Scheme of line of sight on CCD.

position of the telescope. It was assumed that the area below the horizon was dark while the area above was bright. By adjusting the elevation angle of the telescope, the movement of the shadow line over the fibres and subsequently over the CCD can be observed. This information is then utilised to ascertain the elevation angles of the individual CCD lines relative to the telescope's elevation.

The total FOV of the instrument can be mapped on the CCD lines (stripes), with the elevation angle set such that both θ_1 and θ_N look at the horizon in one scan sequence, the elevation angle θ_i for each line L_i, can be calculated using Equation 4.1.

$$\theta_i = \frac{L_i - L_H}{L_1 - L_N} \cdot (\theta_1 - \theta_N)$$

Equation 4.1

Based on Equation 4.1, each stripe corresponds to a specific elevation angle that has been binned together for use in the campaign, as detailed in Table 4.1. Since the instrument FOV does not extend up to 90°, the telescope must be directed toward the zenith for zenith measurements. This approach allows for the utilisation of most of the CCD, as there is minimal variation in the light reaching the CCD lines in this direction.

Table 4.1: Line of sight definition.

Elevation angle (°)	Pixel binned range
-2	182-185
1	170-172
2	163-166
3	159-162
4	155-158
6	146-149
8	137-140
15	102-116
30	31-56
90	100-170

4.3.5 Spectral Calibration

A light source emitting spectrum at discrete wavelengths was utilised to calibrate the instrument's response to light. At the entrance of the spectrometer, a rectangular opening called the slit directs the light to the grating disk, here the shape of the incoming light is transformed into a form that approximates a Gaussian curve, particularly by the grating, diffraction and collimation properties of the spectrometer, as illustrated in Fig. 4.11. This shaped curve is known as the instrumental spectral response function (ISRF). The width of the slit determines the shape of the intensity distribution, specifically, a narrower slit produces a better resolution Gaussian curve. However, narrowing the width of the slit results in a smaller signal being collected, which in turn decreases the signal-to-noise ratio (SNR). To address this issue, a technique known as convolution was employed to compare high-resolution measured spectra of a monochromatic light with the lower resolution produced by the instrument's slit function.
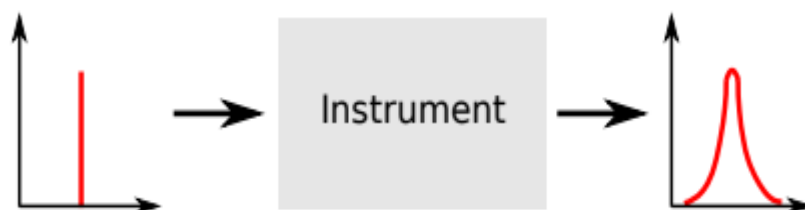
Fig. 4.11: Gaussian curve for monochromatic light source. (Ostendorf, 2017)

For a low resolution wavelength (λ) and a high resolution wavelength (λ') this can be shown mathematically in Equation 4.2, with $I(\lambda)$ as the resulting low-resolution spectra, $I_o(\lambda')$ as the high resolution spectrum and $R(\lambda - \lambda')$ the ISRF.

$$I(\lambda) = \int I_o(\lambda') \cdot R(\lambda - \lambda')d\lambda' \qquad \text{Equation 4.2}$$

4.3.5.1 ISRF Measurement Set-up

The characterisation of the ISRF was done using a mercury-cadmium (Hg-Cd) lamp), Fig. 4.12 a), The lamp, positioned in front of the telescope and shielded to prevent the telescope from atmospheric and other light sources, Fig. 4.12 c), contains plasma that
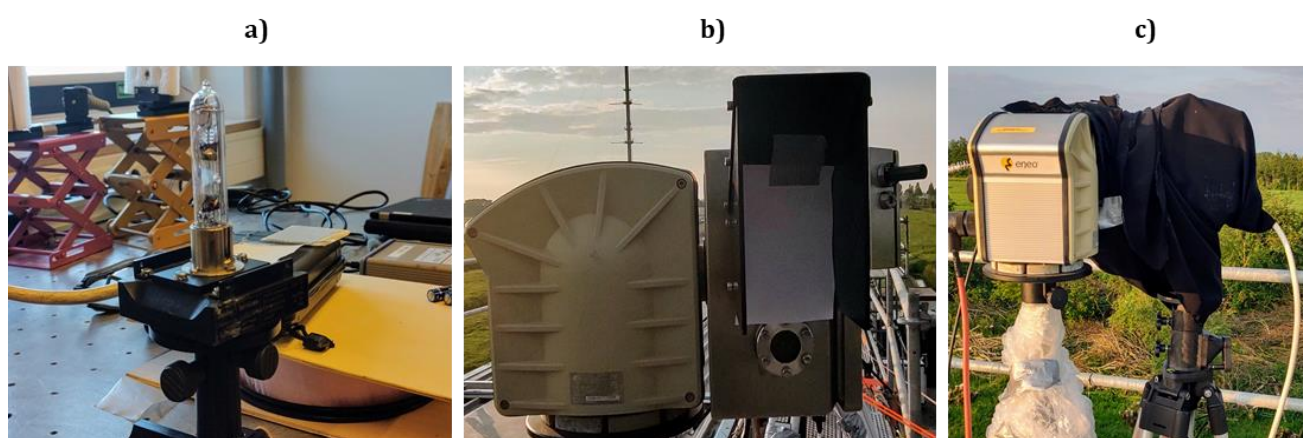
Fig. 4.12: a) Hg-Cd lamp, b) white paper for signal homogeneity, c) lamp-telescope insulation

heats slowly to produce a discrete spectrum. To achieve a homogeneous distribution of the signal into the fibers, a white piece of paper was placed at the telescope window, Fig. 4.12 b). The signal transmitted through the fibers was broadened by the instrument's slit
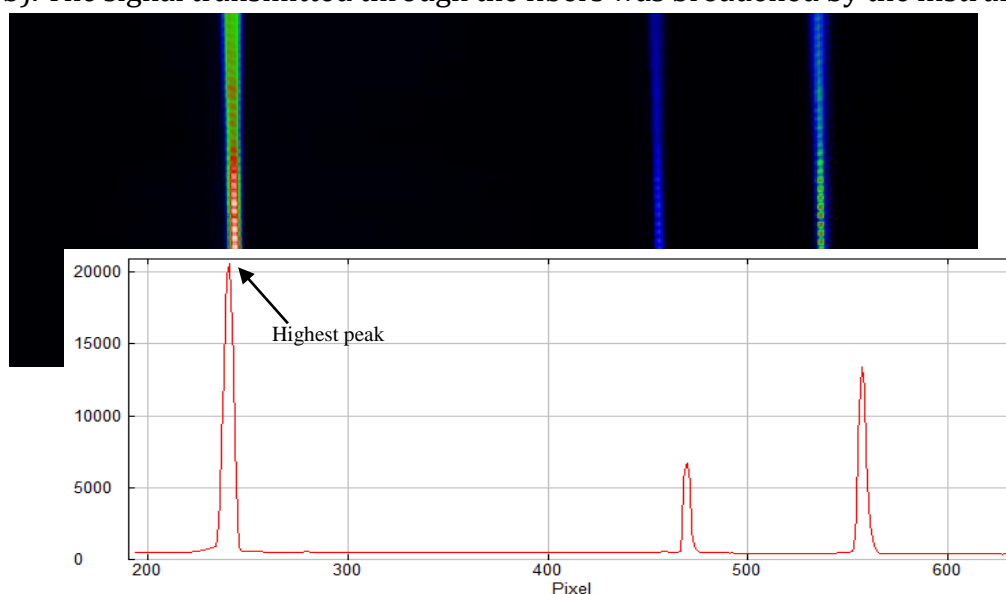
Fig. 4.13: (background) CCD image and (foreground) Spectral lines of Hg-Cd measurement.

function before being recorded on the CCD. The full width at half maximum (FWHM) of the resulting Gaussian curve represents the instrument's ISRF.

Among the peaks measured in Fig. 4.13, the highest peak, which is around 436 nm, was chosen and replicated at every point on the CCD. This peak was fitted with a Gaussian full-width half-maximum (FWHM), as shown in Fig. 4.14. The peaks at the edges deviate more from the Gaussian curve than the center does. This presents a potential problem because the FWHM is kept constant when evaluating the convolution of trace gases in the atmosphere.
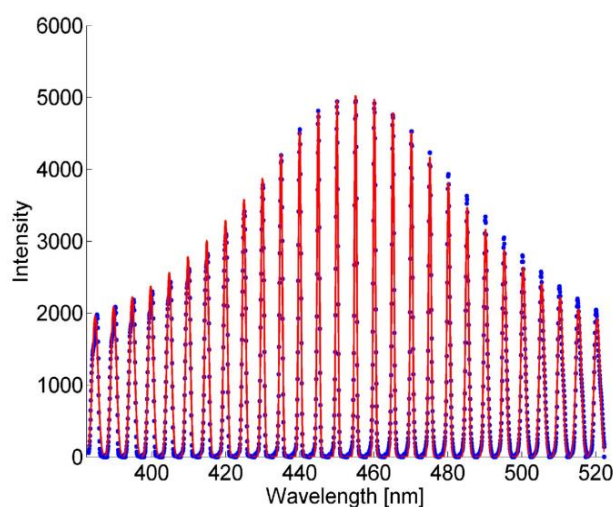
Fig. 4.14: Fitted Gaussian of the Hg-Cd peak (red) and the reproduced peaks (blue) as function of wavelength, (Ostendorf, 2017).

5   Comparison with IUP Bremen MAX-DOAS

As mentioned in 1.1, one of the key aims of the intercomparison was to validate and provide information on the instruments' performance. This section discusses the comparison and regression plots of IMPACT and IUP Bremen MAX-DOAS measurements during the intensive phase. The result is presented in two parts, the first deals with the elevation scans and the azimuthal directions while the second part presents the horizon scans of the instruments.

5.1   Instruments Settings

Specific settings were assigned for the retrieval of target species, although some instruments retrieve more species than others, Table 5.1 shows the common settings used for IMPACT and IUP Bremen MAXDOAS during the semi-blind intercomparison.

Table 5.1: DOAS setting used by IMPACT and IUP Bremen.

Target species	NO_2, O_3, O_4, and H_2O
Wavelength range	425-490 nm
Fraunhofer reference spectra	Daily noon reference spectrum (11:35 - 11:50) UTC
Cross-sections:	
NO_2 (298 K)	Vandaele et al. (1998) with I_0 correction (SCD of 10^{17} molecules/cm^2)
O_3 (223 K)	Serdyuchenko et al. (2014)
O_4 (293 K)	Thalman and Volkamer (2013)
H_2O	HITRAN2012 (Rothman et al., 2013)
Ring	Pseudo-absorber (Chance and Spurr, 1997; Wagner et al., 2009)
Polynomial degree	Order 5 (6 coefficients)
Intensity offset	Constant

5.2   Key Differences

In contrast to the MAX-DOAS instrument, which measures one elevation angle at a time, the IMPACT instrument employs imaging capabilities that allow it to simultaneously observe and measure multiple elevation angles. This simultaneous measurement allows for faster measurements and thereby enhances the detection of temporal variations in NO_2 concentrations, providing a more dynamic analysis of atmospheric conditions. However, this advantage introduces two significant challenges: precise pointing of the instrument and the issue of smear, both of which can affect the accuracy and reliability of the measurements.

5.2.1   Prevention of Smear

The absence of a shutter between measurements and readout poses a challenge in the read-out process of the CCD. As the individual lines of the CCD are read out sequentially by shifting them vertically into the read-out register, illumination of these lines continues throughout this process. This continuous illumination is problematic only in imaging instruments because each CCD line captures light from a different part of the sky. The connection between specific lines and their intended elevation angles is disrupted during read-out, leading to a phenomenon known as "smear." The severity of this effect is influenced by the ratio between exposure time and read-out time, longer exposure times relative to read-out times minimise the issue.

Fig. 5.1: (left) IMPACT telescope window as on May 30, (right)
partial covering using black insulation tape installed.

To address this problem, a solution was implemented that involves reserving a portion of the CCD specifically for read-out. Since the shifting of the stripes' data occurs at a rate

that exceeds the readout process, data is rapidly shifted into this designated area before the sequential reading of the measurement lines occurs. By preventing light from illuminating this area (see Fig. 5.1), the adverse effects of smear are minimised. However, since more than half of the CCD is utilised for measurements, only the lower portion is safe from smear. The upper part still experiences illumination from light coming from unintended directions, which means that while the solution mitigates some issues, it does not eliminate them. Consequently, this method eliminates the need for smear correction in the acquired spectra for lower elevation angles. However, corrections were not applied to the spectra obtained at higher elevation angles.

The impact of smear prevention was evaluated through a horizon scan conducted over an elevation range from -2° to 5°, comparing measurements taken with and without the designated read-out area. During the unmasked measurement, smear correction was applied as outlined in 3.5.2, whereas it was deactivated for the other measurement conducted with the mask. Fig. 5.2 illustrates the intensity as a function of elevation angle for both scenarios.
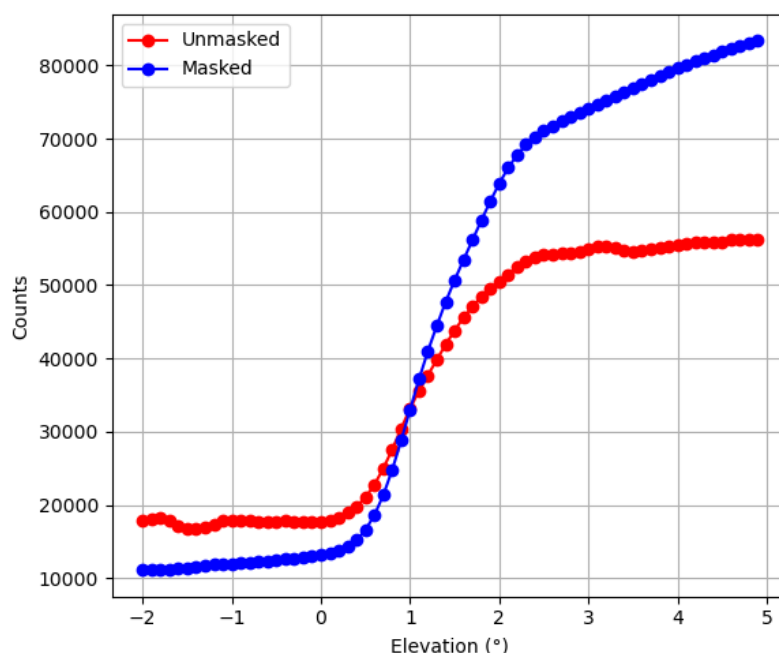
Fig. 5.2: Horizon scan with smear and without smear correction.

In the smear-corrected measurement (red curve), a noticeable drop in intensity is observed compared to the non-smear-corrected measurement (blue curve). This suggests an overestimation of the correction applied to subtract the erroneously acquired light. Additionally, the non-corrected measurement displays a more gradual intensity

gradient, effectively preserving the profile of the scan from dark to bright conditions. Furthermore, ripples present below the horizon and above 3° in the curve of measurements without the mask were absent in the curve of measurements with the mask. This indicates that light from other directions can affect the intensity of some CCD lines when using a wider illumination window.

5.2.2 Field of View (FOV)

The FOV of the IMPACT instrument was determined through a horizon scan measurement conducted on the roof of the IUP building in Bremen on a clear, sunny day. During this measurement, two areas on the CCD corresponding to elevation angles of -2° and 1° recorded different intensity levels as the telescope was adjusted to various elevation angles. A derivative of the intensity distribution was then calculated and plotted in Fig. 5.3.

The curve for the 1° elevation angle (green) is narrower than that for the -2° angle (orange), yet both curves remain wider than the FOV of the IUP Bremen MAX-DOAS, as shown in Fig. 5.4. This difference in FOV significantly influences the DSCDs of NO_2. This will be discussed later in this chapter.

A similar methodology was employed to determine the FOV of the IUP Bremen MAX-DOAS instrument, utilising a typical horizon scan from a day during the CINDI-3 campaign.
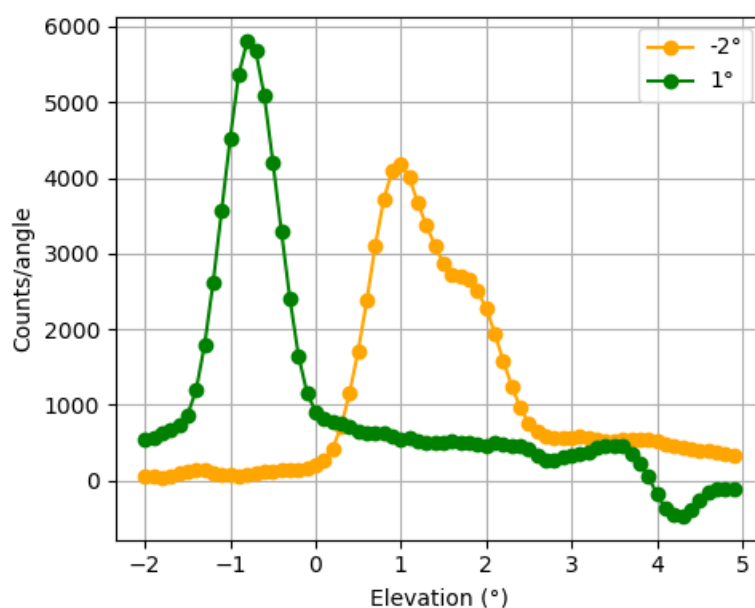
Fig. 5.3: -2° and 1° field of view of IMPACT.
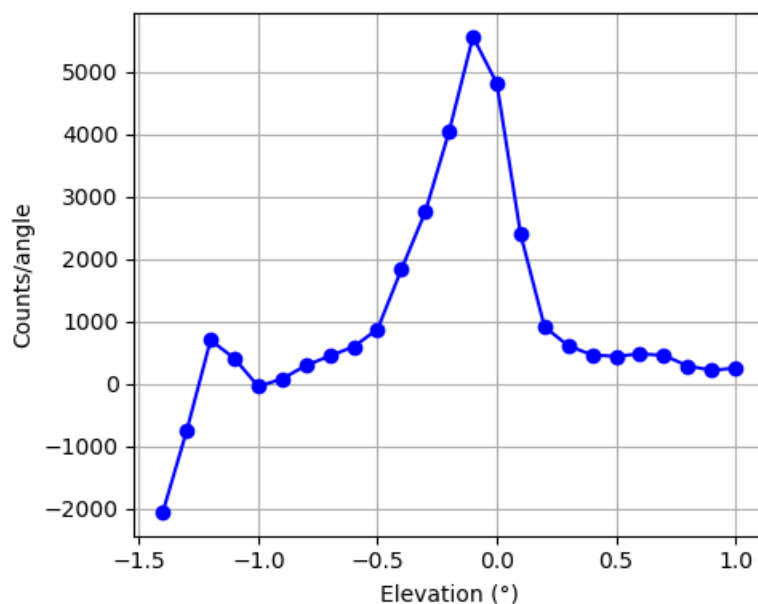
Fig. 5.4: IUP Bremen MAX-DOAS field of view.

5.3 Elevation Scans

Measurements were conducted at various elevation angles, including -2°, 1°, 2°, 3°, 4°, 5°, 6°, 8°, 15°, and 30°, with the primary pointing direction set at 287°. The results of these measurements are presented in this section. For each measurement taken with the MAX-DOAS instrument, a corresponding measurement from the IMPACT instrument, collected at a similar time, was selected for comparison. Since IMPACT captures data at multiple elevation angles simultaneously, the data is filtered to retain only the elevation angle that closely matches the one used in the MAX-DOAS measurement. Furthermore, from the DOAS analysis, any fitting with a root mean square (RMS) value exceeding 0.003 was excluded from the comparison to ensure data quality.

5.3.1 Regression Plots

Fig. 5.5 presents a regression plot for data collected on June 6, encompassing all elevation angles at the primary azimuthal direction. The blue dots which represent DSCDs of NO_2 measured by the IMPACT and IUP Bremen MAX-DOAS instruments, are plotted along the red regression line. The regression line exhibits a consistent trend across elevation angles from 1° to 6°, indicating a strong correlation in this range matching the 1:1 black dashed line. Although, the slope becomes comparatively larger at elevation angles of 8°, 15°, and 30°, it exceeded 0.9 for most elevation angles indicating a strong agreement among the measurements from the two instruments, although the intercepts vary significantly across different angles.

The correlation coefficient for almost all elevation angles is r ≥ 0.94, demonstrating a strong linear relationship among the two instruments. However, the measurement at -2° presents an exception, with a correlation coefficient of r = 0.91. This lower value suggests a weaker relationship, likely due to the instrument's observation below the horizon, where measurements are significantly affected by scattering from various surfaces. This scattering can introduce variability and reduce the reliability of the data collected at this specific angle.
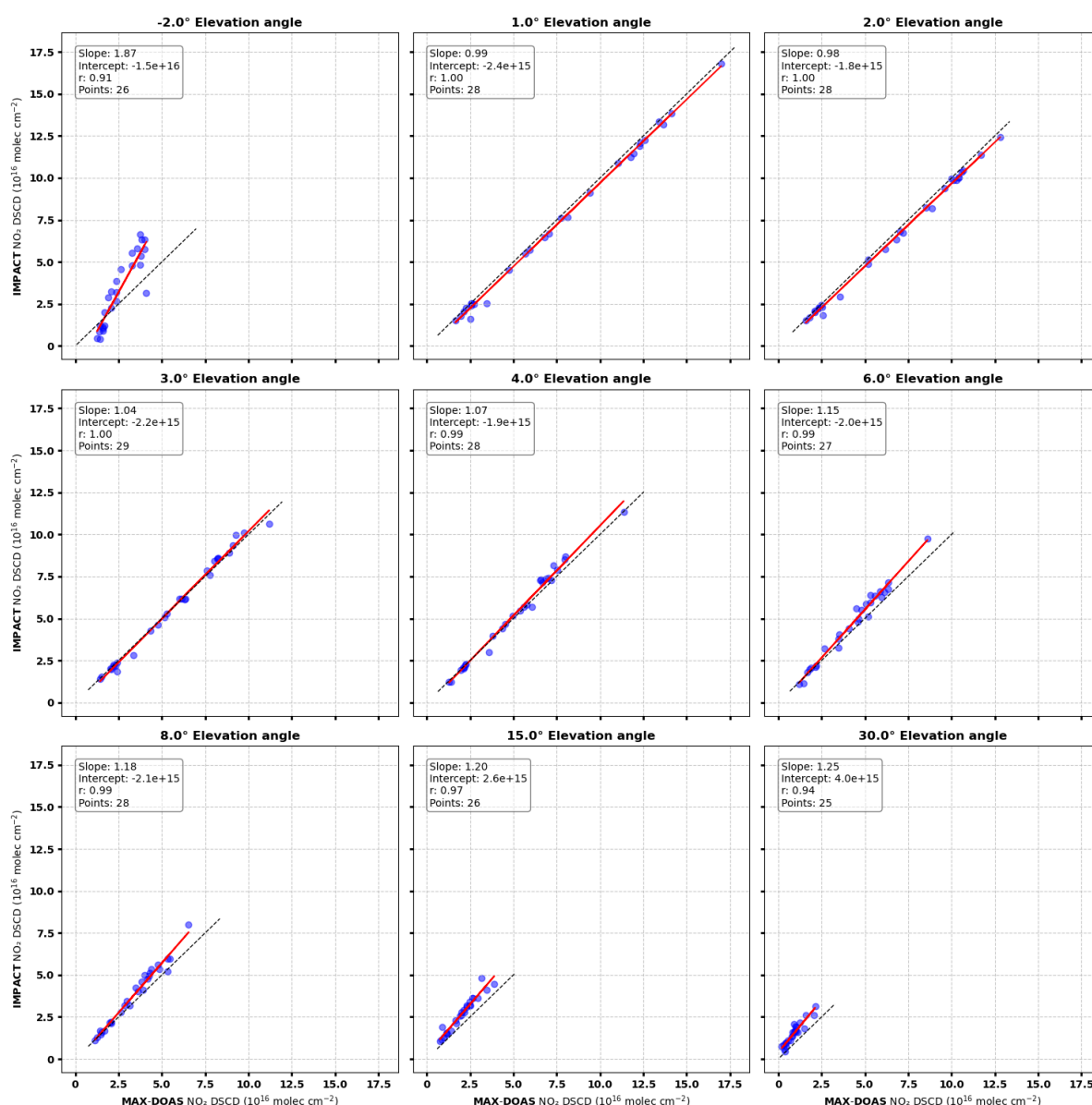
Fig. 5.5: Regression plots of NO₂ DSCDs for IMPACT and IUPB MAX-DOAS across various elevation angles at 287° azimuth on June 06, 2024 showing slope, intercept, correlation coefficient and number of data points.

Additionally, a noticeable decline in the DSCDs of NO_2 is observed as the elevation angle increases, with the minimum values recorded at 30°. This trend supports the assumption that light travels a longer path in the troposphere at lower elevations than at higher elevation angles and AMF is considerably smaller under these geometry. Additionally, there is a decrease in the number of data points at higher elevation angles, suggesting potential instrument saturation due to increased light intensity, adversely impacting measurements at these angles.
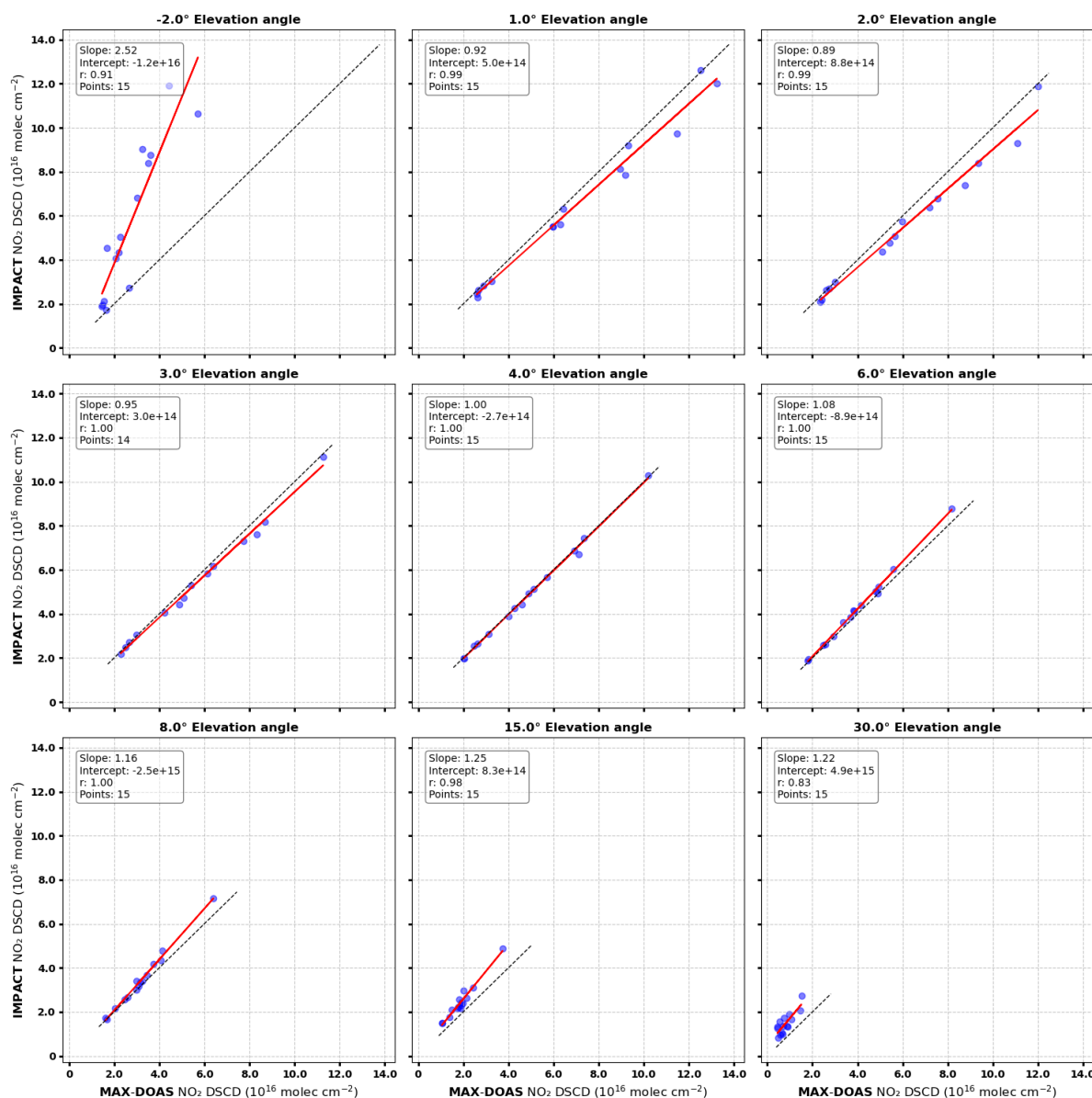
Fig. 5.6: Regression plots of NO_2 DSCDs for IMPACT and IUPB MAX-DOAS across various elevation angles at a secondary azimuth (50°) on June 06, 2024 showing slope, intercept, correlation coefficient and number of plotted data.

Among the secondary azimuthal directions, 50° was analysed and presented in Fig. 5.6, revealing a strong correlation that follows a similar trend to that described in Fig. 5.5.

Measurements taken in this direction, which corresponds to a different viewing angle than the primary direction, further confirm the strong agreement in slope, with a maximum offset of 25% observed at the 15° elevation angle. However, the intercept values exhibit a notable divergence; while the main direction displayed negative intercepts, this alternate direction shows more positive values.

The scatter points in Fig. 5.7 represent the correlation coefficient, slope, and intercept for each day, with colours indicating different elevation angles. A strong agreement in the slope is observed across nearly all days for the measured angles above the horizon, which is similarly reflected in the intercept values. The error bars associated with the slope and intercept indicate the uncertainty of the slope and the intercept, respectively.
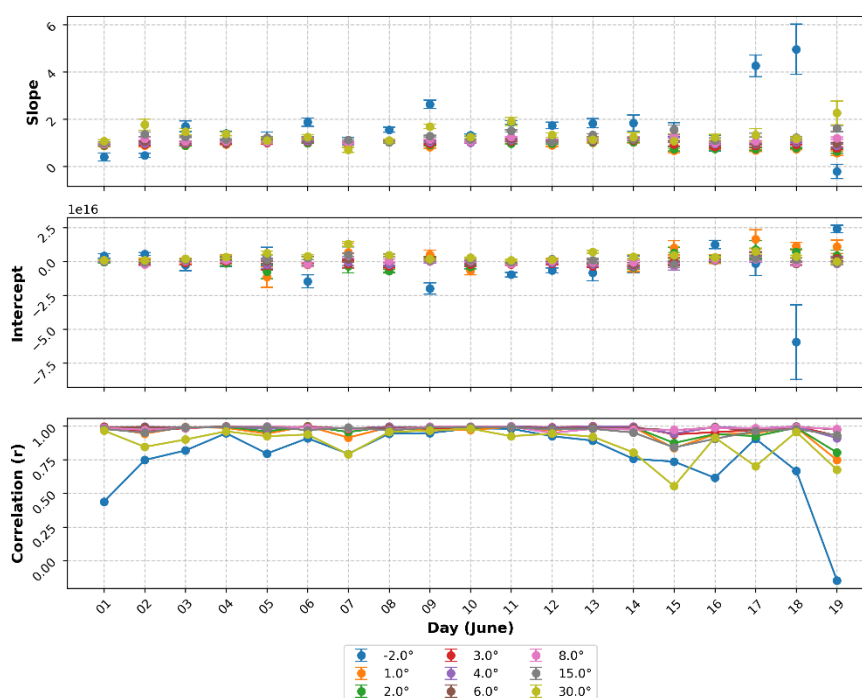
Fig. 5.7: Correlation coefficient, slope and intercept for the intensive phase 287° azimuth.

Analysis of the data from June 1 to June 13 reveals an improving trend in correlation, which appears to diminish during the final week of the campaign. This relaxation in correlation is particularly pronounced at the 30° elevation angle.

5.3.2   Time Series Analysis

As with all other comparison plots, the IMPACT instrument has an advantage by providing significantly more measurements per unit of time in each specified direction compared to the MAX-DOAS. These numerous measurements were then filtered to select those that closely matched the timing of the MAX-DOAS measurements.

Fig. 5.8 presents the temporal evolution of NO_2 abundance for the same day depicted in Fig. 5.5, encompassing all elevation angles. The solid blue line represents the NO_2 DSCDs measured by the IMPACT, while the dashed orange line corresponds to the measurements from the MAX-DOAS instrument.
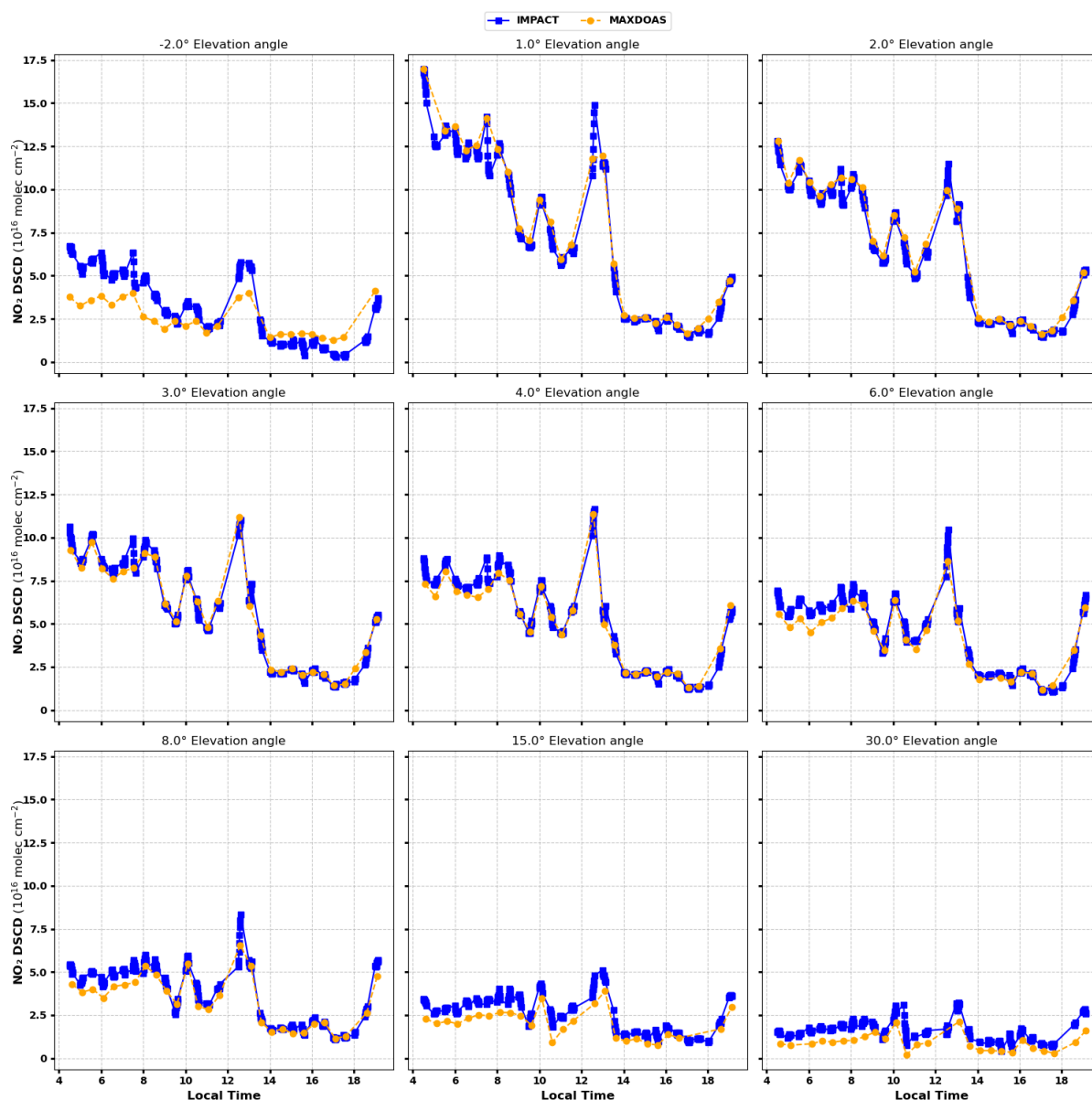
Fig. 5.8: Diurnal variation of NO_2 DSCDs measured by IMPACT and IUPB MAX-DOAS across various elevation angles at 287° azimuth on June 06, 2024.

The data reveal that higher NO_2 DSCDs were recorded in the morning at lower elevation angles, followed by a gradual decline throughout the day maintaing observable variability, with a subsequent increase observed in the evening. Notably, an unusual peak in NO_2 levels was detected during the afternoon, suggesting the presence of an emission plume within the observed azimuthal direction.

Aside from this afternoon peak, the curves indicate minimal temporal variation in NO_2 DSCDs at higher elevation angles , this was due to the less concentration of NO_2 at these elevation angles . In this range, MAX-DOAS measurements tended to present lower NO_2 levels than IMPACT, whereas IMPACT presented similar feature at lower elevation angles. This discrepancy of the intercept highlights the differing sensitivities of the two instruments to NO_2 concentrations across varying elevation angles.

5.3.3 Zenith-Sky

After every elevation sequence, both instruments proceed with immediate zenith-sky measurements to ensure the closest synchronisation of I_0 as outlined in the DOAS method. The data analysis of these measurement is presented in this section.
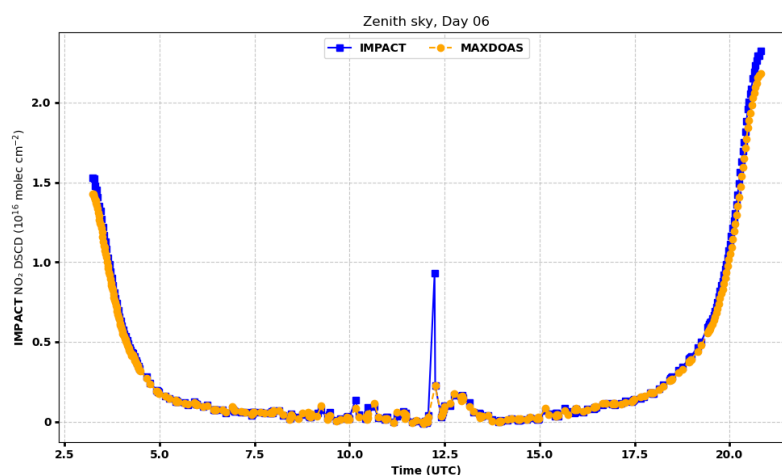
Fig. 5.9: Zenith-sky measurements as a funtion of time on June 6, 2024.

Figure 5.10 illustrates the typical NO_2 DSCDs obtained from zenith sky measurements, with the solid blue line representing data from the IMPACT instrument and the dashed orange line corresponding to the MAX-DOAS instrument. Both instruments recorded relatively low DSCDs of NO_2 in the zenith sky. A gradual decrease in concentration is observed throughout the day, attributed changes in AMF due to changes in SZA, which changes the length of the light path in the stratosphere. Following sunset, a gradual increase of NO_2 is noted in the evening hours, which explains the dependency of DSCDs on light path. Additionally, a small peak in concentration is observed in the afternoon, coinciding with similar peaks detected at other elevation angles on the same day.

Fig. 5.10 displays the zenith-sky regression plots for four selected days during the intensive measurement phase. The correlation coefficients indicate a very strong linear relationship, with values of r = 1.0 for all days analysed. Among these, June 1 exhibits the

best slope compared to the other days. Additionally, the intercept across all days shows a stronger correlation overall.

Despite the little variations in slope and intercept, the DSCDs of NO_2 remained relatively consistent across the sampled days, indicating stability of instruments during this period.
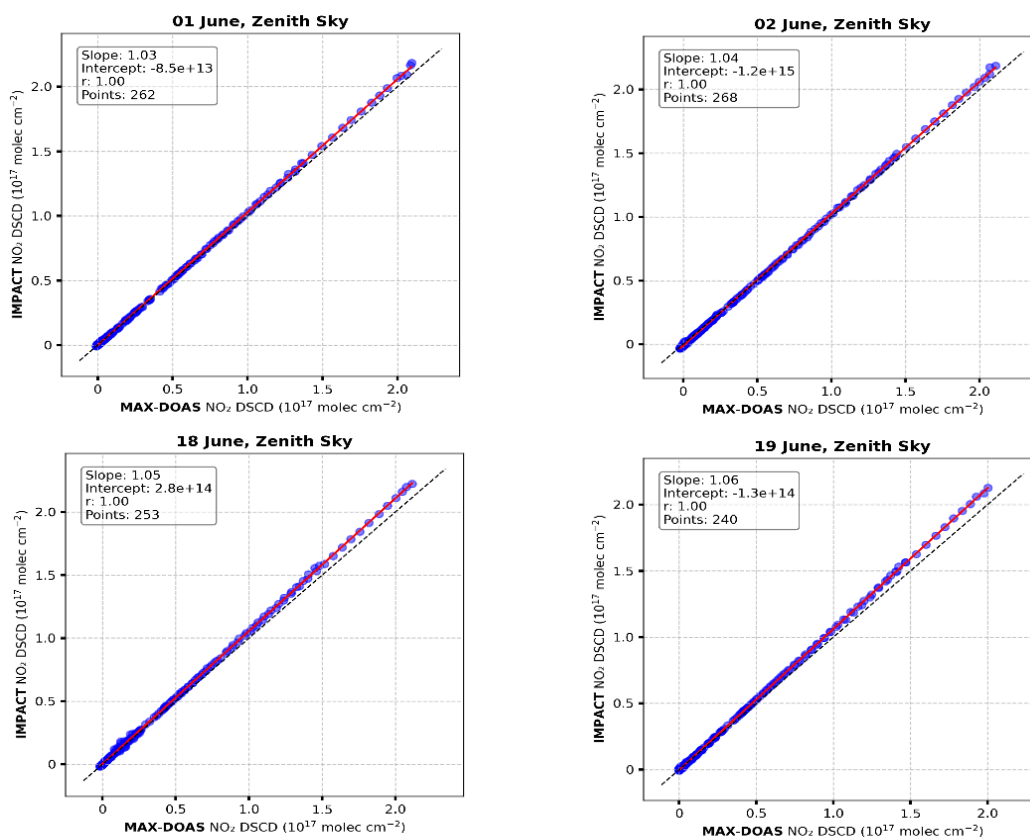
Fig. 5.10: Zenith-sky regression plots of selected days from intensive phase.

5.4 Azimuthal Scans

To investigate azimuthal variability, all MAX-DOAS instruments collected measurements at a specific elevation across various azimuthal directions. Similarly, the IMPACT instrument utilised the same azimuthal directions, however, as an imaging instrument, it gathered data across all elevation angles. For this comparison, the appropriate elevation angle was selected from the IMPACT data to align with the measurements taken by the MAX-DOAS instruments.

The results of the azimuthal scans which include 0° (north), 70°, 121°, 200°, 245°, and 287°, are presented in this section. While the primary pointing direction has the lowest horizon, several other directions faced obstacles, such as trees, that affected

measurements at elevation angles of 1° and 2° as shown in Fig. 5.11. Consequently, the decision was made to adopt 3° as the target elevation angle instead of the previously used 2°, which had been employed as a test during the pre-commencement phase.

The analysis focuses on data acquired twice every hour for these azimuthal directions, providing insights into how environmental factors influence measurements and enhancing our understanding of plume emissions across different directions.
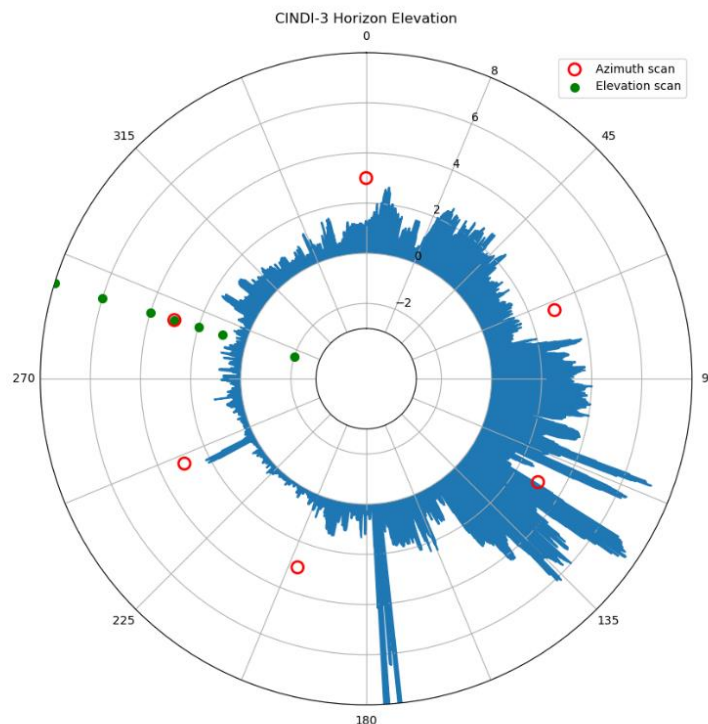
Fig. 5.11: Polar plot of the CINDI-3 horizon's elevation near the measurement site, (CINDI-3 Coordination Team, 2024).

The blue shaded peaks in Fig. 5.11 indicate the obstructions near the measurement site, as inferred from a basic image processing analysis. The red circles mark the 3° elevation in the selected azimuthal directions. Despite efforts to avoid these obstacles during measurements, the 121° direction was not entirely free from obstructions, which may have influenced the data collected in that azimuth.

5.4.1 Regression Plots

Fig. 5.12 displays a regression plot for data collected on June 12 at an elevation angle of 3° for the selected azimuth. The blue dots represent the DSCDs of NO_2 measured by both the IMPACT and IUP Bremen MAX-DOAS instruments, plotted along the red regression line.
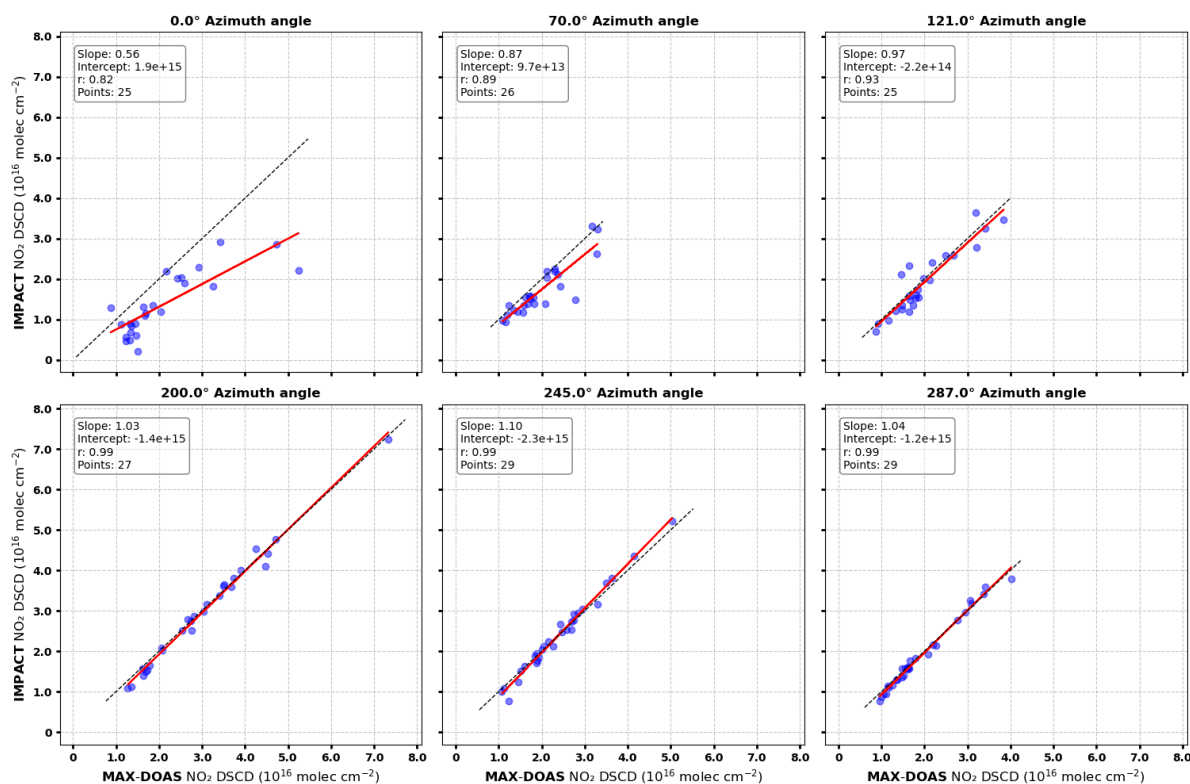
Fig. 5.12: Regression plots of NO₂ DSCDs for IMPACT and IUPB MAX-DOAS across various azimuth angles at 3° elevation angle on June 12, showing slope, intercept, correlation coefficient and number of data points.

The slope and correlation coefficient for the 0° azimuth are 44% and 12% away from the optimum value of 1.0, indicating a weak agreement in this direction. In contrast, other azimuthal directions exhibit strong correlations, with coefficients exceeding 0.9, except for the 70° direction, which has a coefficient of 0.89.

Additionally, the azimuthal directions of 200°, 245°, and 287° show higher DSCDs of NO₂ compared to other directions, highlighting variations in atmospheric conditions across different angles.

The scatter points illustrated in Fig. 5.13 represent the correlation coefficient, slope, and intercept for each day, with distinct colours indicating different azimuthal directions. There is significant variability in both the slope and intercept observed in the due north direction (0°) across nearly all days. This variability is particularly pronounced in the error bars associated with the 0° and 121° azimuthal directions.

In contrast, other azimuthal directions exhibit more consistent results, however, the 121° direction also shows variability due to obstructions similar to those encountered at 0°. The varying correlation coefficients reflect differences in the strength of relationships

observed on different days, suggesting that atmospheric conditions are dynamic and can change significantly over time.

These findings highlight the importance of considering azimuthal direction and atmospheric conditions when interpreting the instruments performance. The analysis underscores that both the slope and intercept are subject to fluctuations influenced by many conditions, which can affect the overall reliability of measurements taken under this conditions.
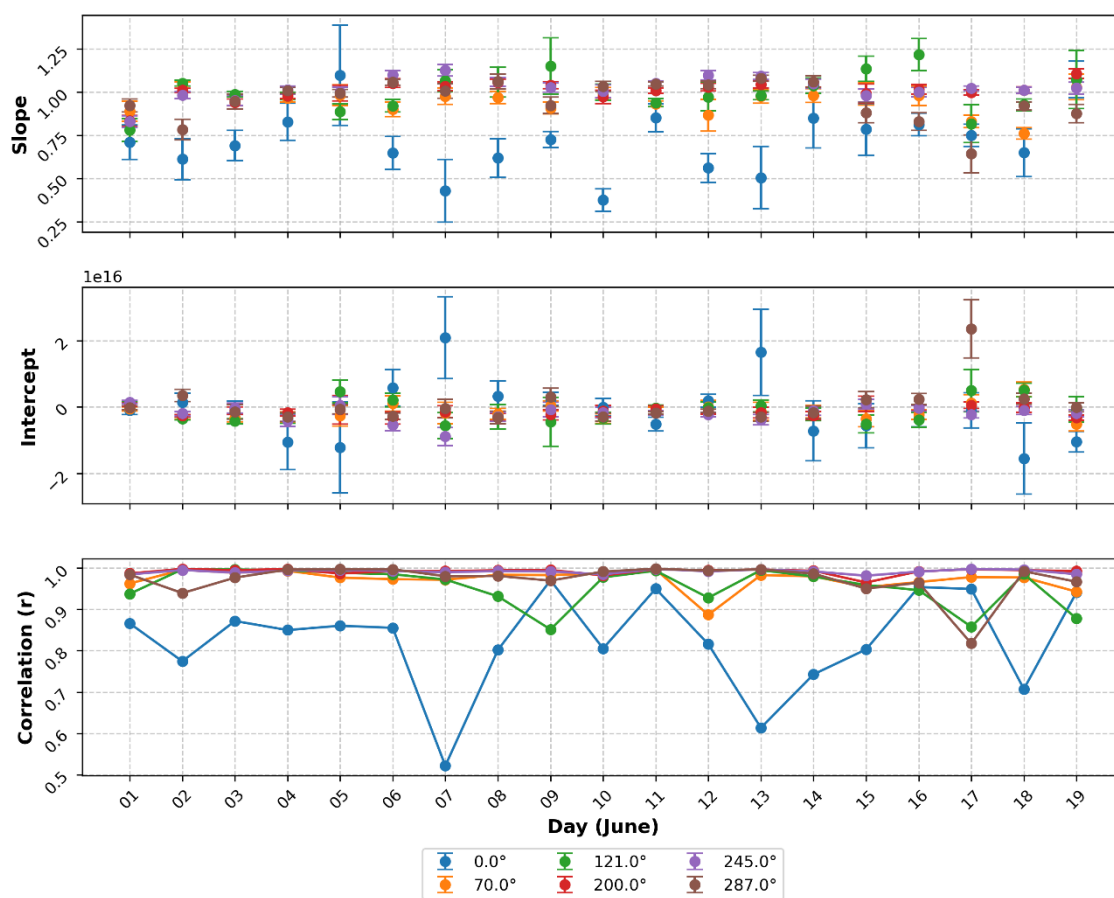
Fig. 5.13: Correlation coefficient, slope and Intercept for the intensive phase azimuthal scans.

5.4.2 Time Series Analysis

The concentration of NO$_2$ changes rapidly over time at lower elevations, this variation which is not limited to a certain direction was analysed. Fig. 5.14 shows the diurnal variation of NO$_2$ over different azimuth direction.

The MAX-DOAS measurements at the 0° direction revealed two peaks in the morning and evening, both of which were underestimated by the IMPACT instrument. In contrast, the

morning peaks at 200° and 245° were recorded by both instruments, indicating a more consistent performance in these azimuthal directions.
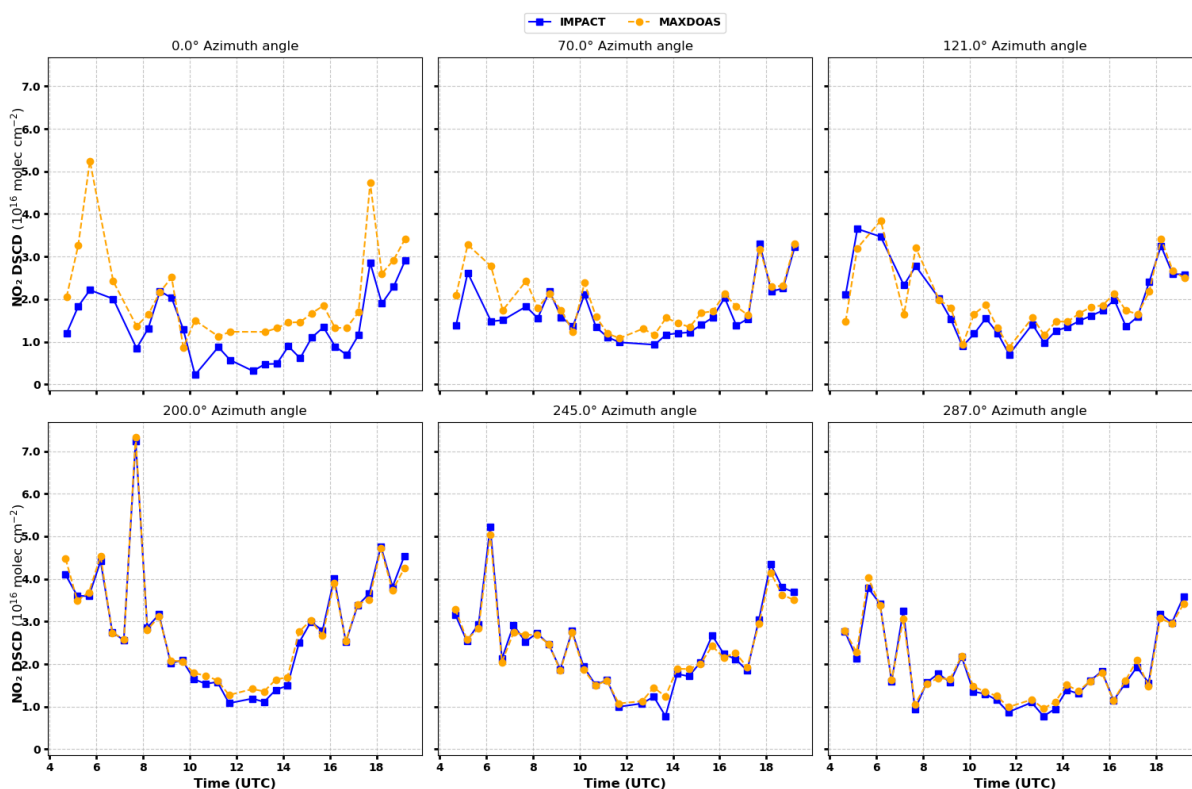
Fig. 5.14: Diurnal variation of NO_2 DSCDs measured by IMPACT and IUPB MAX-DOAS at 3° elevation angle across various azimuthal direction on June 12, 2024.

As illustrated in Figure 5.13, the NO_2 DSCDs across all directions do not exhibit significant discrepancies, however, the IMPACT instrument consistently underestimates NO_2 concentrations in all measured directions. This underestimation is attributed to the differences in measurement sensitivities between the two instruments.

Fig. 5.15 presents a plot comparing the slope and intercept across all days as a function of the azimuth angle, with a colour bar showing normalised error which is the deviation from the optimum values. The performance at 0° is notably the poorest, while the 200° direction exhibits the strongest agreement between the instruments throughout the campaign period. This enhanced correlation may be attributed to the 200° direction having fewer obstacles above the horizon, allowing for more accurate measurements and less interference.
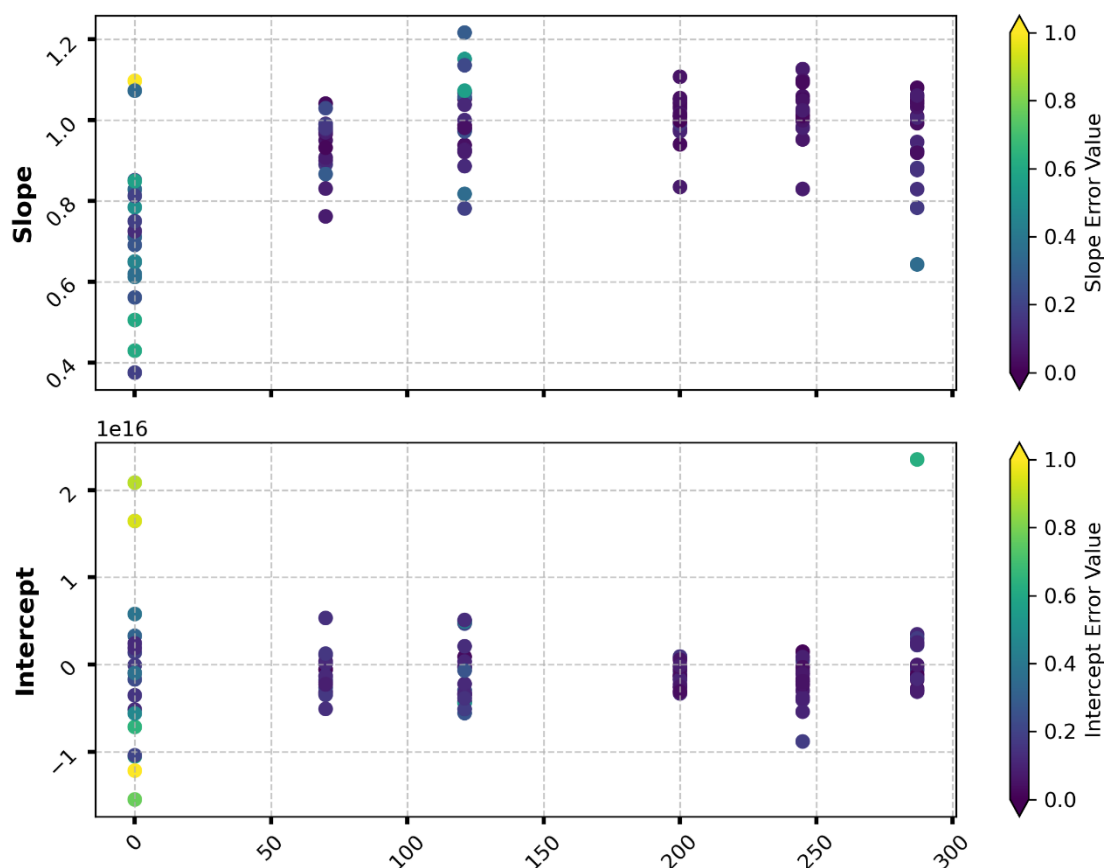
Fig. 5.15: Slope and intercept of the azimuth angles during the whole campaign.

5.5 Discussion of IMPACT and IUP Bremen MAX-DOAS comparison

The regression plots demonstrate a robust linear relationship between the DSCDs of NO_2 measured by the IMPACT and IUP Bremen MAX-DOAS instruments, with correlation coefficients exceeding 0.9 across all elevation scans. This strong correlation indicates that both instruments are effectively capturing similar atmospheric conditions.

However, the intercept values exhibit significant variability across different elevation angles, suggesting that while the overall trend remains consistent, there are specific discrepancies in baseline measurements between the two instruments. These differences may arise from factors such as instrument calibration, environmental conditions, and observational geometry.

At lower elevation angles, the consistent trend in slope indicates a strong correlation between the instruments. Conversely, large values of slopes at higher elevation angles may suggest potential issues such as instrument underestimation or overestimation from the instruments, which affects measurement accuracy. The variability introduced by the wider FOV of the IMPACT instrument results in larger error bars in some slope and

intercept values. This increased uncertainty complicates data interpretation and may lead to less reliable conclusions regarding atmospheric NO_2 concentration which is very large near surface and decreases with altitude.

A noticeable decline in DSCDs of NO_2 is observed as the elevation angle increases, with the lowest values recorded at 30°. This trend may be attributed to shorter light paths and lower concentrations of NO_2 at higher elevations. The secondary azimuthal directions also exhibit a strong correlation, however, differing intercept values indicate directional variability in the measurements.

Scattering from surfaces and heightened light intensity at lower elevation angles can significantly impact measurement reliability in optical systems. As the elevation angle decreases, the likelihood of encountering surface irregularities and environmental obstacles such as trees or structures increases. These factors can lead to multiple scattering events, where light reflects off surfaces before reaching the detector.

Clouds, particulate matter, and aerosols significantly affect the reliability of these measurements. The presence of clouds can scatter and absorb incoming light, leading to inaccuracies in the data collected by instruments. When aerosols are present, they can serve as cloud condensation nuclei (CCN), influencing cloud formation and properties. This interaction can alter the reflectivity and lifetime of clouds, resulting in complex effects on light transmission.

Moreover, particulate matter can introduce variability in measurements due to its ability to scatter light in unpredictable ways. As aerosol concentrations fluctuate with meteorological conditions such as humidity and precipitation their impact on light scattering and absorption can lead to significant uncertainties in measurements.

Morning measurements reveal higher concentrations of NO_2 at lower elevation angles, followed by a gradual decline throughout the day and an unusual peak in the afternoon. This peak suggests the presence of an emission plume, which has not been investigated but has been identified at various elevation angles. Minimal temporal variation in NO_2 concentrations is noted at higher elevation angles, aside from the aforementioned afternoon peak.

Both instruments conduct zenith-sky measurements following each elevation sequence to synchronise their reference intensity. The data from these measurements show low

NO$_2$ DSCDs in the zenith sky, with a gradual decrease during daylight hours attributed to SZA which determines the AMF, followed by a slight increase in concentrations during the evening. The zenith-sky regression plots for selected days indicate strong correlations (r = 1.0), reflecting consistency and stability of the instruments' performance.

Regarding azimuthal scans, strong correlations are observed in most directions except for 0° and 121°, where significant variability is noted. Notably, the 200° direction demonstrates the strongest agreement between instruments during the entire campaign period, highlighting its enhanced reliability for capturing atmospheric NO$_2$ concentrations.

6   360° Hemispheric Scans

This chapter introduces the analysis of the free scan sequence, which was conducted hourly across all instruments. The IMPACT instrument utilises this sequence to perform hemispherical scans, measuring the full 360-degree azimuth in increments of 10 degrees. Each scan is configured to last for 10 minutes, providing approximately 16 seconds of integration time for each directional measurement, with an exposure time of about 1.6 seconds per measurement. This systematic approach enables the detection of temporal variability in NO_2 concentrations, facilitating a comprehensive analysis of meteorological and atmospheric conditions. The results obtained from these scans are presented and discussed in detail in this chapter, highlighting their significance in understanding NO_2 dynamics and overall air quality.

6.1   Hourly Scans

The figures presented below illustrate the hourly distribution of NO_2 DSCDs from 4:00 to 19:00 UTC for selected days. The y-axis represents the elevation angle, while the x-axis indicates the azimuth direction. The colour gradient on the accompanying colour bar reflects the concentration levels of NO_2.

Common features can be observed in Fig. 6.1, Fig. 6.2 and Fig. 6.3. The 0° and 100° to 160° azimuthal directions are densely populated with trees, a meteorological tower is situated at an azimuth of 170°, while the KNMI mast is located at 320°. An instrument is also positioned within the 340° direction. These features are prominently visible within the field of view (FOV) of the IMPACT instrument, particularly at lower elevation angles, highlighting their potential impact on measurements. White gaps in the graphs indicate missing data, primarily resulting from instrument saturation.
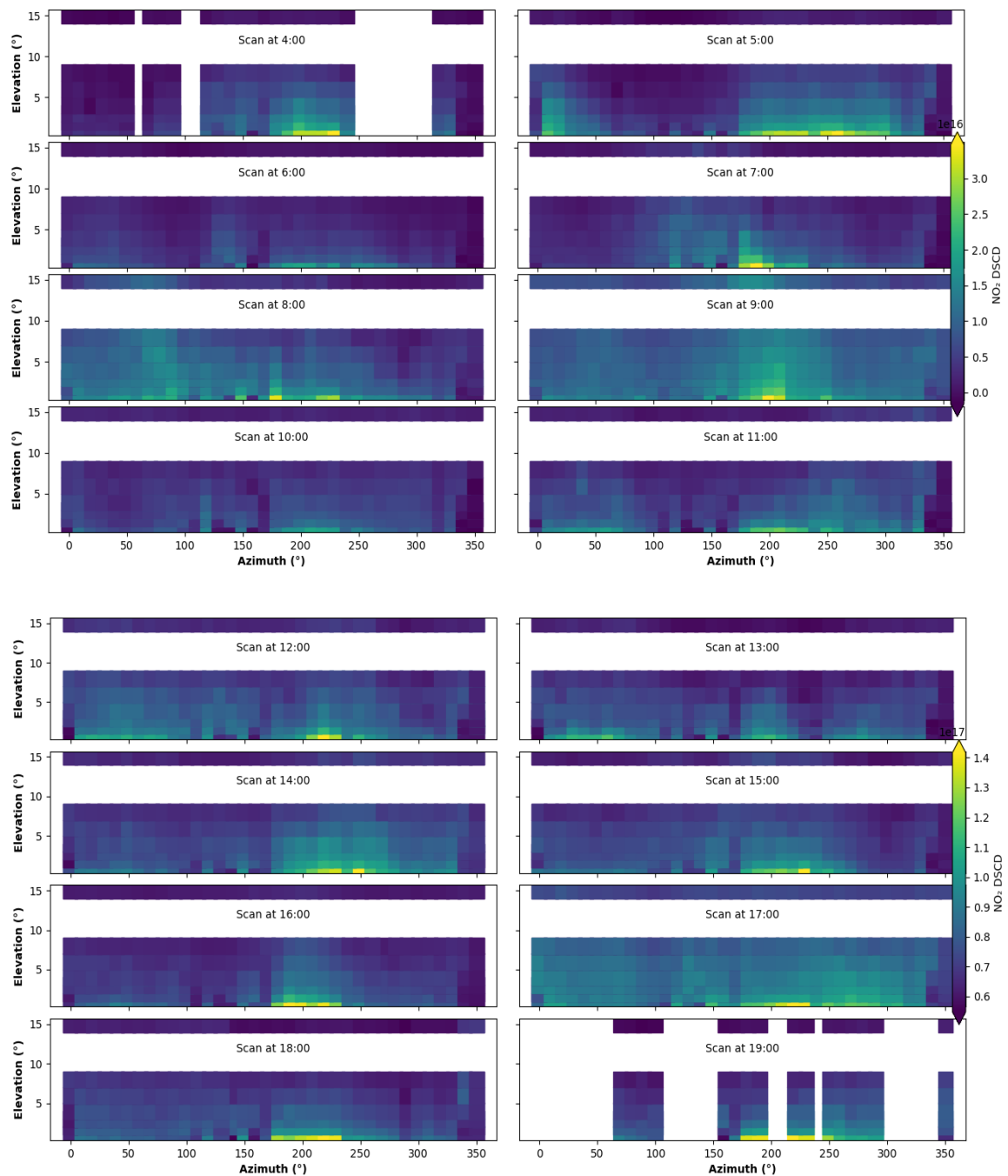
Fig. 6.1: Hemispherical scan of NO₂ DSCD for June 12, 2024.
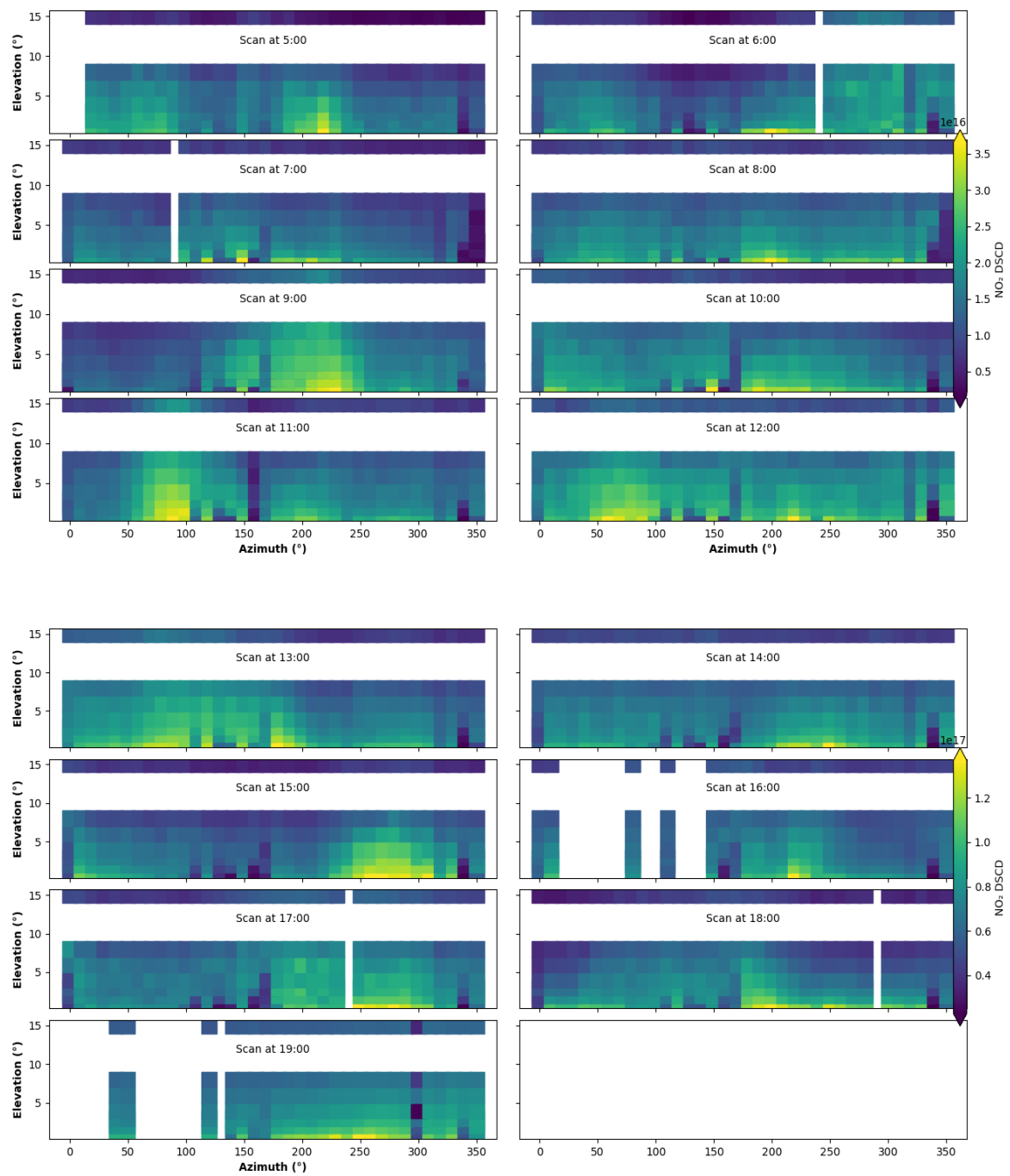
Fig. 6.2: Hemispherical scan of NO₂ DSCD for June 15, 2024
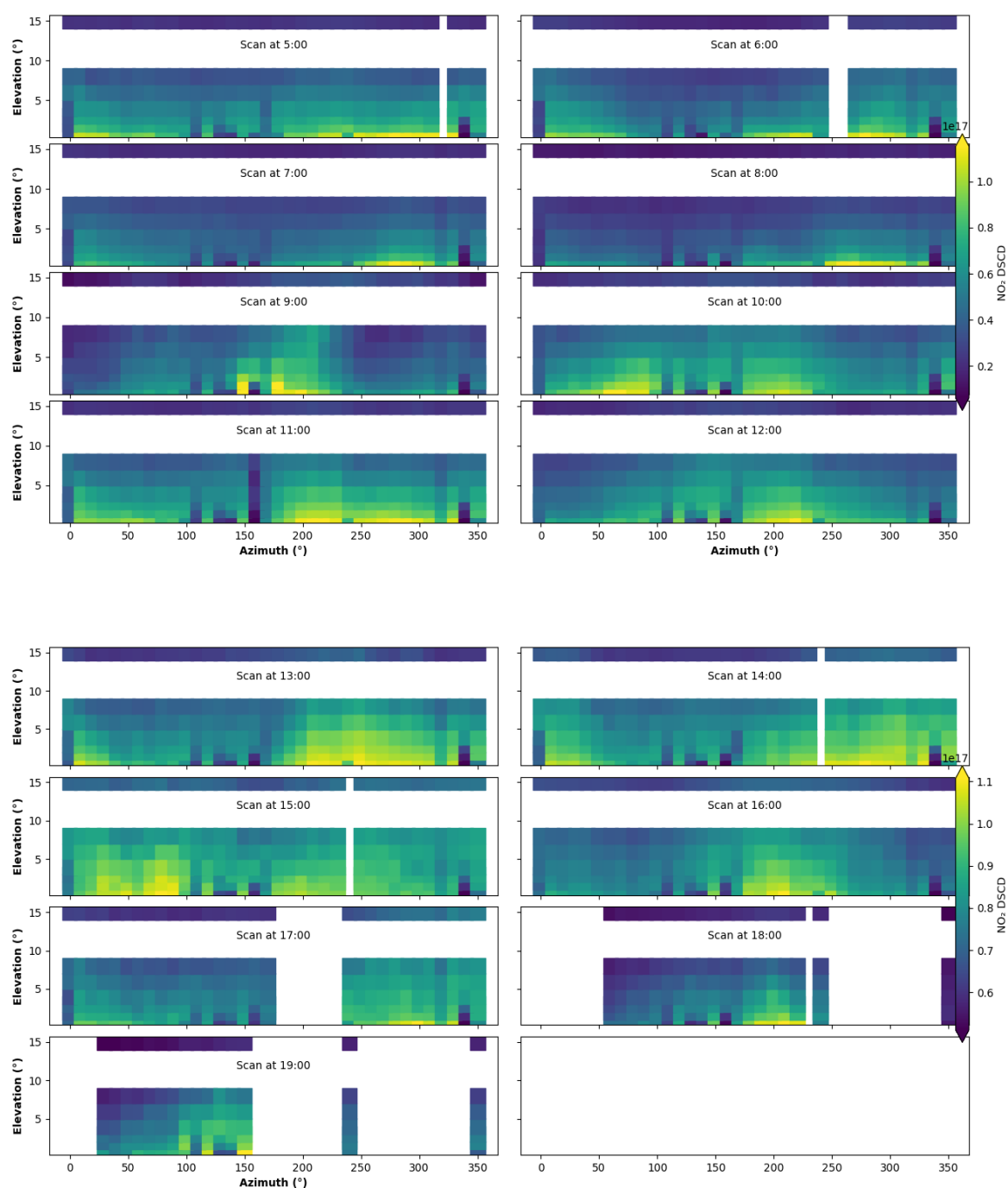
Fig. 6.3: Hemispherical scan of NO₂ DSCD for June 18, 2024

On the morning of June 12 (Fig. 6.1), maximum values of NO₂ DSCDs peaking at about 3.5×10^{16} molec/cm² were observed at lower elevations which is close to the ground between 4:00 and 5:00 UTC. A decrease in concentration was noted over the subsequent hour, likely attributed to reactions with water vapour and OH radicals, resulting in the formation of HNO₃ as described in Equation 2.12. Following sunshine, a continued decline of NO₂ DSCDs levels was recorded as AMF keep changing with change in SZA, with a low

concentrations maintained during the day until an increase was observed in the evening, peaking at around 1.5×10^{17} molec/cm^2. These fluctuations in NO$_2$ DSCDs were attributed to the variation of the AMF, which is typically smaller during the day and due to proximity with emission sources which decrease with increase in altitude.

Starting at 5:00 UTC on June 15 (Fig. 6.2), a distinct distribution pattern of NO$_2$ was observed, characterised by a large DSCDs in the azimuthal range of 180° to 230° after 9:00 UTC. Larger NO$_2$ values were recorded at higher elevations, reaching up to 8°. A subsequent peak NO$_2$ DSDC of 4.0×10^{16} molec/cm^2 was detected in the 70° to 100° direction after 11:00 UTC, followed by another peak in the 250° to 300° range after 15:00 UTC. These peaks were not observed during the earlier hours of the day, however, both areas of elevated NO$_2$ are attributed to traffic emissions and the proximity to the nearby Cabauw city, where vehicular activity is a significant source of NO$_2$.

In the evening hours, a more homogenised distribution of NO$_2$ was noted across all directions, with a maximum NO$_2$ DSCD of 1.3×10^{17} molec/cm^2 recorded at lower elevation angles. This shift in distribution patterns highlights the dynamic nature of NO$_2$ concentrations throughout the day and underscores the influence of various atmospheric conditions on its behaviour.

On June 18, elevated NO$_2$ values were recorded, reaching approximately $1.1\text{-}1.2\times 10^{-17}$ molec/cm^2 in the morning and evening. A uniform distribution of NO$_2$ was observed at an elevation of 1° during the morning across all directions, except where views were obstructed. Measurements commenced at 5:00 UTC, however, an unusual peak in NO$_2$ concentration was noted in the 150° to 200° azimuthal range at approximately 2° elevation by 9:00 UTC. This peak later thinned to the left and right directions throughout the day. The frequent saturation of the instrument on both June 15 and June 18 indicates illuminated clouds during these observations, which likely facilitated NO$_2$ DSCDs readings. The saturation events suggest that the instrument was operating near its maximum intensity detection limits.

6.2 Daily Average

This section presents the daily averaged scans depicted in 6.1, elevation angles have been converted to altitude using methodologies outlined by (Sinreich, Merten, Molina, & Volkamer, 2013) and (Seyler, et al., 2017). These techniques leverage the DSCDs of O$_4$ to

calculate the light path responsible for the absorption of trace gases, thereby enabling altitude determination through geometric considerations. The plots included in this section will provide an overview of the daily maximum and minimum concentrations of NO_2, facilitating a clearer understanding of factors associated with the variations and distribution patterns throughout the observed period.
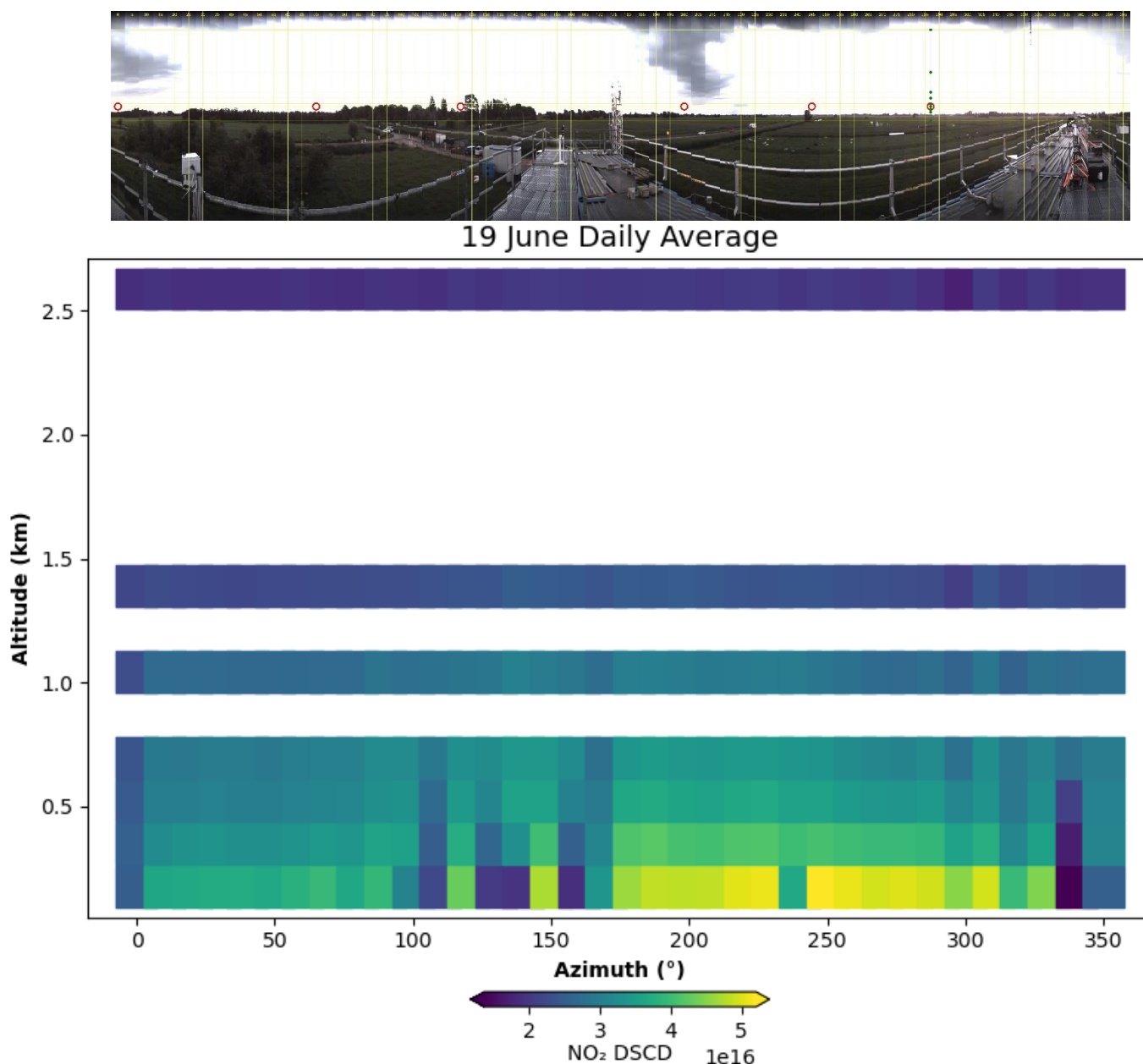

Fig. 6.4: Mean DSCDs of NO_2 for hemispheric scan on June 19, 2024 and panorama picture showing horizon horizontal red line), elevations(horizontal yellow lines), azimuth directions (vertical yellow lines), (CINDI-3 Coordination Team, 2024).
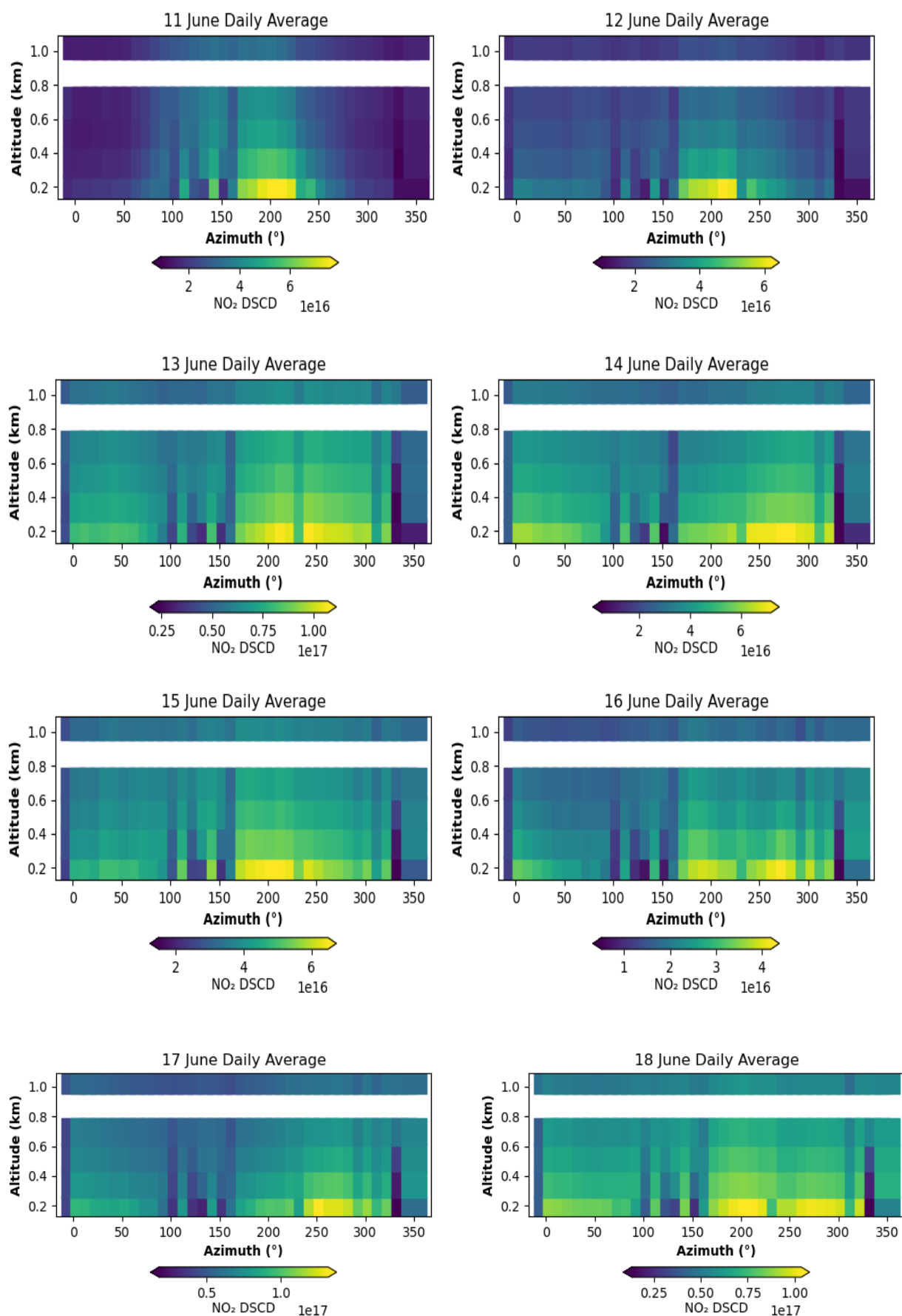
Fig. 6.5: Mean DSCDs of NO₂ for hemispheric scans on June 11-18, 2024.

The panoramic image in Fig. 6.4 illustrates the physical features observed on-site during the hemispherical scans. Accompanying this image is a graph displaying the mean values of NO_2 DSCDs distributed concerning altitude on June 19. The data indicate that elevated NO_2 DSCDs in order of 5.5×10^{16} molec/cm^2 were recorded primarily in the azimuthal range of 180° to 310°, reaching a maximum altitude of 500 m that day. This information indicates the spatial distribution of NO_2 and highlights specific directions where concentrations were notably enhanced in this case, the Schoonhoven city.

The mean values from other days presented in Fig. 6.5 indicate recorded enhancements in NO_2 concentrations along a similar azimuthal direction, except June 14 and June 18, when notable values were observed in additional directions. This suggests that the peaks detected during specific hours were associated with particular plumes rather than a continuous source of emissions.

To fully understand the behaviour of these plumes, it is essential to consider the influence of directional winds, as they play a critical role in the movement and dispersion of pollutants. Overall, very little NO_2 was detected at altitudes above 1500 meters, indicating that significant concentrations are primarily confined to lower elevations.

6.2.1 Validation of NO_2 Enhanced Values

Since the DSCD of NO_2 is influenced by various factors beyond its atmospheric profile, it is essential to validate this distribution through multiple approaches. Factors such as light intensity and path length can significantly affect the elevated NO_2 values observed in hemispherical scans. To ensure a more precise interpretation of the NO_2 distribution, other trace gases that are typically found both near the surface and at higher elevations and measured along the same light path are utilised for validation.

In this context, both O_4 and water vapour H_2O are employed as reference trace gases. By comparing the DSCDs of these gases, we can better understand the atmospheric conditions affecting NO_2 measurements and confirm the reliability of the observed distributions. This multi-gas approach enhances the accuracy of our analysis and provides a more comprehensive understanding of the factors influencing NO_2 concentrations in the atmosphere.
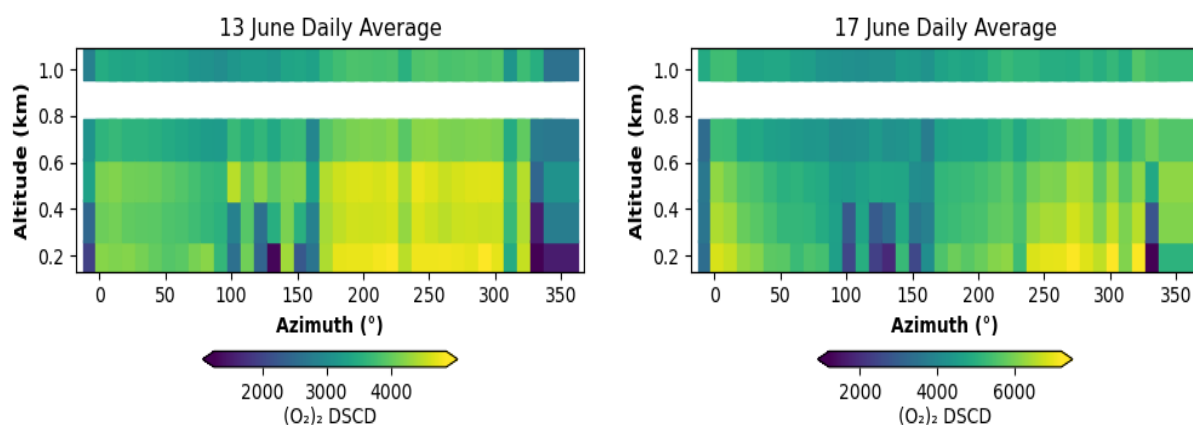
Fig. 6.6: Mean DSCDs of O_4 for hemispheric scans on 13 and 17 June, 2024

Fig. 6.6 illustrates the distribution of O_4 with altitude, a maximum DSCD of O_4 reaching 5000×10^{40} molec^2/cm^5 on June 13 and 6500×10^{40} molec^2/cm^5 on June 17 were recorded. Notable values of O_4 were observed in azimuthal directions where NO_2 was not detected on the same days, indicating that the enhancement of NO_2 DSCDs is due to enhancement of NO_2 concentrations rather than atmospheric light path. Conversely, the presence of O_4 was observed at both near-surface levels and higher altitudes. A similar trend was noted for water vapour, as illustrated in Fig. 6.7. On June 13, the maximum DSCDs of water vapour was recorded at approximately 500 meters above the ground. However, on June 17, higher values were observed close to the ground, paralleling the pattern seen for O_4.
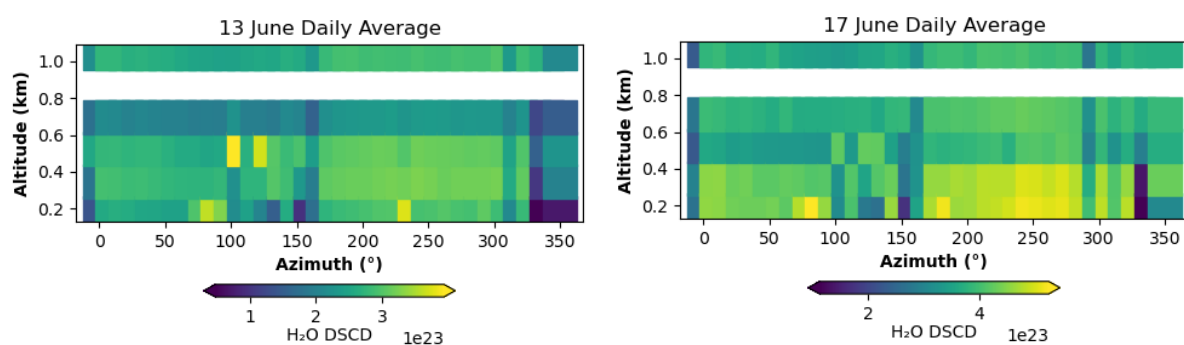

Fig. 6.7: Mean DSCDs of H_2O for hemispheric scans on 13 and 17 June, 2024.

6.3 Discussion of Hemispheric Scans

The hourly distribution of NO_2 DSCDs from 4:00 to 19:00 UTC over selected days is presented. Common features emerge, particularly in the azimuthal directions of 0° 170°, 320°, 340° and 100° to 160°. NO_2 DSCDs recorded varied from day to day with a minimum

average of 4.5×10^{16} molec/cm^2 on June 16 and a maximum average of 1.5×10^{17} molec/cm^2 on June 17.

The subsequent temporal variation observed across the hours might be likely attributed to reactions with water vapour and hydroxyl (OH) radicals that led to nitric acid (HNO_3) formation and/or O_3 photolysis which produce chemical radicals that destroy NO_2. Another potential cause for the variation is transport by local winds in the surrounding area, which has not been investigated here. These higher evening concentrations were associated with lower elevation measurements, which typically exhibit elevated NO_2 levels that diminish with increasing altitude. Overall, very little NO_2 was detected at altitudes above 1500 m, indicating that significant concentrations are primarily confined to lower elevations.

The peak concentrations were attributed to traffic emissions from the nearby city, highlighting vehicular activity as a significant source of NO_2 or transport events as these are the most common sources of the measured NO_2. Emissions from agricultural activities are among the sources of NO_2 within the neighbouring environment. Periods when the instruments experienced saturation correspond to hours of clear sunshine, bright clouds, sunrise, and sunset.

The findings presented, highlight the complex interplay between local emissions sources and atmospheric dynamics that govern NO_2 concentrations throughout different times of day and environmental conditions.

The analysis of the daily averages indicates that the peaks observed during specific hours were associated with distinct plumes rather than arising from a continuous source of emissions. Nonetheless, emissions were predominantly concentrated in the azimuthal range of 180° to 310°.

7 Summary and Outlook

For the second time, IMPACT was deployed to participate in a semi-blind intercomparison exercise which took place at CESAR remote-sensing site Cabauw aimed at better understanding the measurement technique and data evaluation approaches to enhance air quality monitoring and deepening our understanding of the Earth's atmosphere.

This work introduces the intricate dynamics of atmospheric processes, particularly focusing on the measurement and analysis of trace gases, such as NO_2, using remote sensing techniques. The methods employed during the CINDI-3 campaign showcased the DOAS retrieval techniques using a variety of platforms, including mobile and airborne measurements. The foundational principles of the DOAS technique were elaborated upon, detailing how light extinction due to absorption and scattering is quantified to derive gas concentrations.

The IMPACT instrument consists of three main components, receiving optics, connective optics, and a spectrometer-detector system. The receiving optics include a waterproof telescope with an objective lens and a camera for scene documentation. Light collected by the objective is transported via sorted quartz fibres to an imaging spectrometer coupled with a charge-coupled device. This configuration allows for simultaneous measurement of multiple spectra corresponding to different viewing directions.

The optimal spatial and spectral resolution was achieved through a three-step adjustment process involving CCD alignment to the spectrometer, positioning of the fibre relative to the spectrometer for optimal wavelength resolution, and adjustment of the fibre to the objective to define the field of view. Additionally, optimisation and testing of the instrument in handling the imaging capability were done which included installing filters to prevent saturation and reorganisation of the readout mechanism to speed up the readout of spectra in order of priority, that way it remains less susceptible to smear.

A comprehensive campaign schedule, outlining the measurement sequence and hourly routine for each day, was introduced during the CINDI-3 campaign to guide instrument operation. The reference azimuth direction for comparison was set at 287° west-northwest, with 0° representing North and increasing clockwise. Based on solar position geometry, the daytime measurement period was designated from 4:10 UTC to 19:10 UTC.

Within this timeframe, eight hourly cycles were defined in both the morning and afternoon, including a ten-minute free sequence. Additionally, a noon cycle was scheduled from 11:10 to 12:10, while zenith-sky measurements were conducted for one minute at a time throughout the active hours, from 04:40:00 UTC to 19:09:59 UTC.

Azimuthal calibration was performed using a high-resolution azimuthal scan also called skyline scan. The telescope moved in 0.1° increments to ensure that the KNMI mast was within the instrument's field of view. The knowledge of the position of the mast was used to adjust the azimuth alignment by introducing an offset. A car lamp was set up at a distance of 1.3 km, and its azimuth was determined by finding maximum light intensity during a skyline scan. The telescope elevation angle is adjusted until the lamp moves out of view, allowing for precise alignment. The CCD lines were binned, and lines with similar intensities were binned together and assigned to specific elevation angles, which allowed for accurate identification of FOV.

The measured spectra were converted to slant column files using IUP Bremen DOAS analysis software, these output files were used for the comparison of IMPACT with IUP Bremen MAX-DOAS and hemispheric analysis. Key findings from the analysis demonstrated a high correlation between the instruments in all comparable measurements. However, IMPACT demonstrated a wider field of view which resulted in the underestimation of NO_2 concentration retrieved.

The results of hemispheric scans indicated that NO_2 concentrations were significantly influenced by local emissions sources, particularly in urban areas and traffic ways with notable peaks linked to specific plumes rather than continuous emissions. Additionally, very little NO_2 was detected at altitudes above 1500 m.

Overall, the IMPACT instrument has demonstrated good performance in atmospheric remote sensing, particularly when compared to 3D MAX-DOAS instruments. However, areas for enhancement have been identified, as outlined below:

- **Integration of a custom optical filtering system**: Implement a custom optical filtering system that incorporates multiple neutral density filter options, which can be switched electronically. This would enable real-time adjustments based on varying environmental conditions, effectively addressing saturation issues and enhancing SNR control.

- **Upgrade to fast read-out CCD**: Transition to a fast read-out CCD to improve saturation control. Additionally, a frame transfer CCD would provide both rapid readout and high sensitivity with low readout noise. This upgrade would mitigate smear effects and enhance measurement precision.

- **Broadening the spectral range**: With saturation and smear issues resolved, the instrument's spectral range should be expanded by using a spectrometer with imaging capabilities, even at the edges. This enhancement would facilitate the retrieval of additional trace gases, such as glyoxal ($C_2H_2O_2$) and formaldehyde (CH_2O).

- **Investigating adaptation in diverse climates**: Exploring the adaptation of IMPACT in different climatic conditions would yield valuable insights into its performance across various atmospheric environments. This investigation could help assess the instrument's versatility and robustness in diverse settings, such as Sub-Saharan Africa.

8 Appendices

MAY 2024

SUNDAY	MONDAY	TUESDAY	WEDNESDAY	THURSDAY	FRIDAY	SATURDAY
19 Whit Sunday	20 Whit Monday	21 Build-up/preparation	22 Build-up/preparation	23 Build-up/preparation	24 Build-up/preparation	25 Build-up/preparation
26 Build-up/preparation	27 Intensive phase	28 Intensive phase	29 Intensive phase	30 Intensive phase	31 Intensive phase	1

JUNE 2024

SUNDAY	MONDAY	TUESDAY	WEDNESDAY	THURSDAY	FRIDAY	SATURDAY
26	27	28	29	30	31	1 Intensive phase
2 Intensive phase	3 Intensive phase	4 Intensive phase	5 Intensive phase	6 Intensive phase	7 Intensive phase	8 Intensive phase
9 Intensive phase	10 Intensive phase	11 Intensive phase	12 Intensive phase	13 Intensive phase	14 Intensive phase	15 Intensive phase
16 Intensive phase	17 Optional extension	18 Optional extension	19 Optional extension	20 Optional extension	21 Optional extension	22 Site cleanup
23 Site cleanup	24 Site cleanup	25 Site cleanup	26 Site cleanup	27 Site cleanup	28 Site cleanup	29

Fig. 8.1: Schedule of the CINDI-3 campaign, (CINDI-3 Coordination Team, 2024).

Fig. 8.2: Image showing CINDI-3 measurement site with instruments (outdoor parts) on the roof of the containers housing the instrument (indoor parts).

IMPACT Daily Viewing Geometry
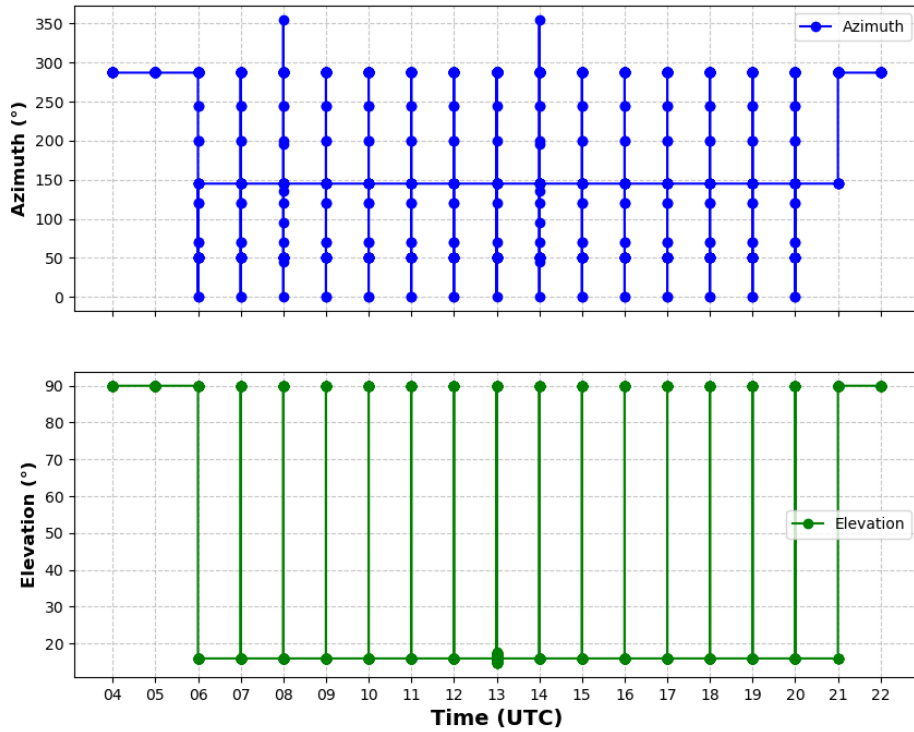
IUP Bremen MAX-DOAS Daily Viewing Geometry
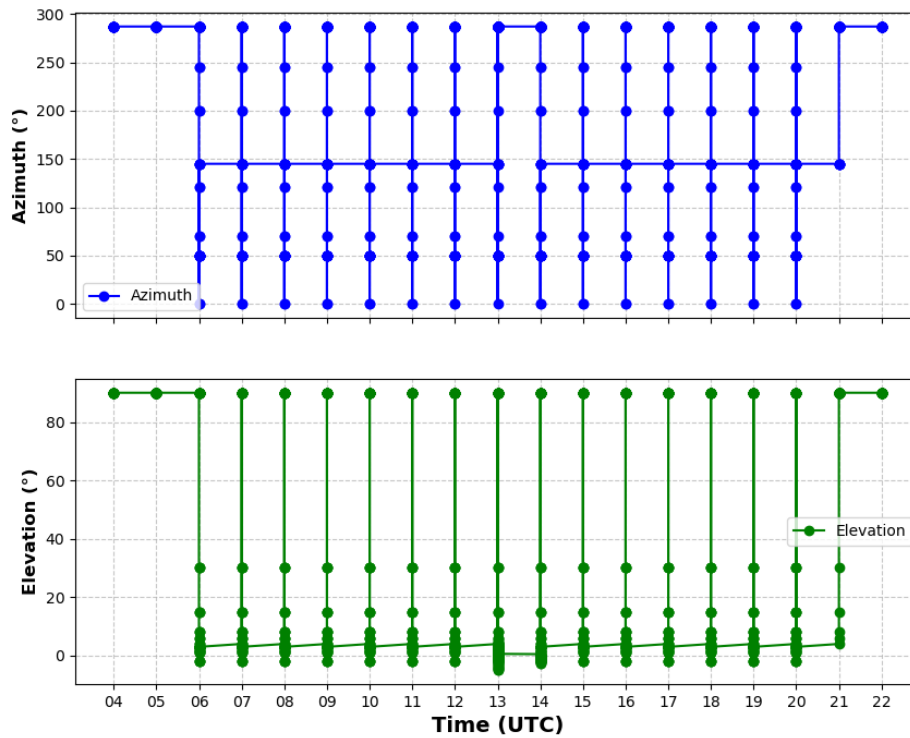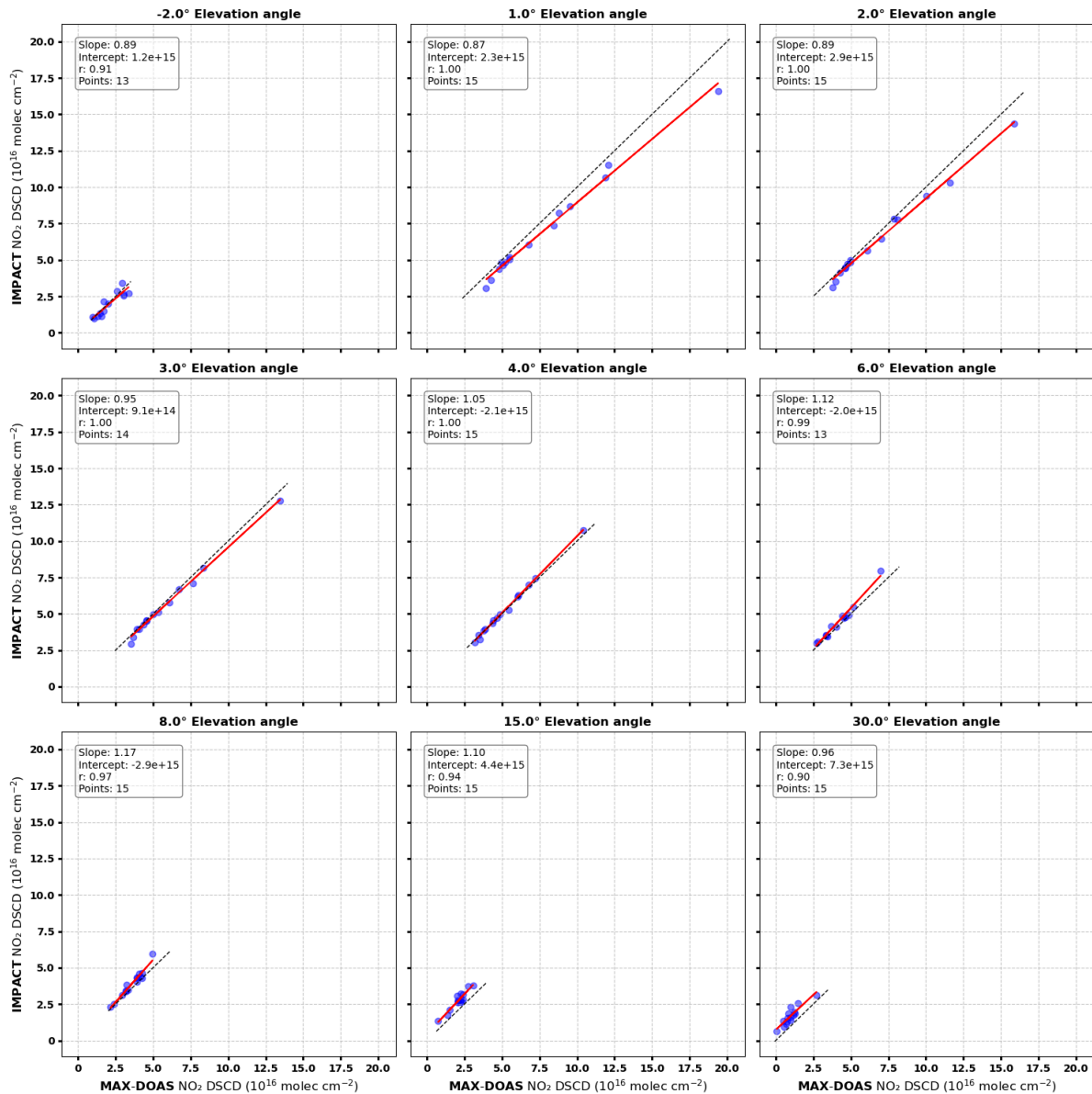

Fig. 8.3: Instruments' daily viewing geometry

Fig. 8.4: Regression plots of NO₂ DSCDs for IMPACT and IUPB MAX-DOAS across various elevation angles at a secondary azimuth (145°) on June 06, 2024 showing slope, intercept, correlation coefficient and number of plotted data.

Table 8.1: Overview of Participating Institutions.

Institute Acronyms	Instrument	Spectral Range	Country
UOM ABOM	SkySpec-1D	300-460 nm	Australia
AIOFM	2D-MAXDOAS	290-450 nm	China
	2D-MAXDOAS	290-420 nm	
	2D-MAXDOAS	290-420 nm	
AIRYX	SkySpec-2D UV	296-459 nm	Germany
	SkySpec-2D VIS	408-553 nm	
AUTH	PHAETHON	280-539 nm	Greece
	DELTA	305-523 nm	
BIRA	2D-MAXDOAS UV	304-383 nm	Belgium
	2D-MAXDOAS VIS	402-543 nm	
	SkySpec-2D UV	296-459 nm	
	SkySpec-2D VIS	408-553 nm	
	NO_2 camera	430-470 nm	
	Aeromobil	195-755 nm	
	Bike-DOAS	280-547 nm	
EVORA	SPATRAM-1 UV	300-400 nm	Portugal
	SPATRAM-1 VIS	400-600 nm	
INTA	RASAS-III	325-445 nm	Spain
ISAC	SkySpec-2D UV	300-405 nm	Italy
	SkySpec-2D VIS	405-565 nm	
IUPB	2D-MAXDOAS UV	305-550 nm	Germany
	2D-MAXDOAS VIS	305-390 nm	
	Car-DOAS 1	406-579 nm	
	Car-DOAS 2	305-550 nm	
	IMPACT	305-550 nm	

	Rapid DOAS	305-550 nm	
IUPH	SkySpec-2D UV	296-459 nm	Germany
	SkySpec-2D VIS	408-553 nm	
	PMAX-DOAS	285-565 nm	
KNMI	SkySpec-1D	300-460 nm	The Netherlands
	Mini-DOAS	290-433 nm	
	Hoffmann	400-600 nm	
	Pandora-1S	280-540 nm	
LATMOS	SAOZ	270-640 nm	France
	Mini-SAOZ 1	270-820 nm	
	Mini-SAOZ 2	270-820 nm	
LBLICK	Pandora-1S	280-540 nm	Austria
	Pandora-1S	280-540 nm	
LMU	SkySpec-1D	300-460 nm	Germany
	SkySpec-1D (Car-DOAS)	300-460 nm	
	SkySpec-2D UV	310-410 nm	
	SkySpec-2D VIS	405-550 nm	
MPIC	Tube-DOAS 1	300-460 nm	Germany
	Tube-DOAS 2	300-460 nm	
PKNU-NIER	AQ-Profiler	280-795 nm	Korea
RAL	SkySpec-2D UV	310-410 nm	United Kingdom
	SkySpec-2D VIS	405-550 nm	
SUWON	SkySpec-1D	300-460 nm	Korea
UNAM	Car-DOAS	356-510 nm	Mexico
UOT	SkySpec-1D	300-460 nm	Canada
USTC	SkySpec-2D UV	310-410 nm	China
	SkySpec-2D VIS	405-550 nm	

Works Cited

CINDI-3 Coordination Team. (2024). *CINDI-3 Campaign Planning Document .* Cabauw: FRM4DOAS.

GERHARDT, I. L. (2006). *Scattering & Absorption of Light by a Single Moleculeunder a Subwavelength Aperture.* Ph.D. dissertation, SWISS FEDERAL INSTITUTE OF TECHNOLOGY ZURICH.

Goody, R. M. (1995). *Atmospheric radiation: theoretical basis.* Oxford university press.

GRAINGER, J. F., & J., R. I. (1962, February). Anomalous Fraunhofer Line Profiles. *Nature, 193*, 762–762. doi:10.1038/193762a0

IUPB DOAS group. (2024, September 26). Retrieved from http://www.iup.uni-bremen.de/doas/

Kreher, K., Van Roozendael, M., Hendrick, F., Apituley, A., Dimitropoulou, E., Frieß, U., . . . Zhao, X. (2020, May). Intercomparison of NO2, O4, O3 and HCHO slant column measurements by MAX-DOAS and zenith-sky UV–visible spectrometers during CINDI-2. *Atmospheric Measurement Techniques, 13*, 2169–2208. doi:10.5194/amt-13-2169-2020

NASA. (2024, October 15). *Ozone layers.* Retrieved from National Institute of Standards and Technology : https://www.nist.gov/image/layersofozone3-copyjpg

Ostendorf, M. (2017). *IMPACTA new ground-based imaging DOAS instrument: Development, participation at the CINDI-2 campaign and first data analysis.* Master's thesis, University of BremenDepartment 01: Physics and Electrical EngineeringInstitute of Environmental Physics (IUP).

Perner, D., Ehhalt, D. H., Pätz, H. W., Platt, U., Röth, E. P., & Volz, A. (1976, August). OH - Radicals in the lower troposphere. *Geophysical Research Letters, 3*, 466–468. doi:10.1029/gl003i008p00466

Peters, E., Ostendorf, M., Bösch, T., Seyler, A., Schönhardt, A., Schreier, S. F., . . . Burrows, J. P. (2019, August). Full-azimuthal imaging-DOAS observations of NO2 and O4 during CINDI-2. *Atmospheric Measurement Techniques, 12*, 4171–4190. doi:10.5194/amt-12-4171-2019

Platt, U., Perner, D., & Pätz, H. W. (1979, October). Simultaneous measurement of atmospheric CH2O, O3, and NO2 by differential optical absorption. *Journal of Geophysical Research: Oceans, 84*, 6329–6335. doi:10.1029/jc084ic10p06329

Revell, L. E., Bodeker, G. E., Smale, D., Lehmann, R., Huck, P. E., Williamson, B. E., . . . Struthers, H. (2012, August). The effectiveness of N2O in depleting stratospheric ozone. *Geophysical Research Letters, 39*. doi:10.1029/2012gl052143

Richter, A. (2024). *DOAS step by step.* Bremen: IUP, University of Bremen.

Seyler, A., Wittrock, F., Kattner, L., Mathieu-Üffing, B., Peters, E., Richter, A., . . . Burrows, J. P. (2017, September). Monitoring shipping emissions in the German Bight using MAX-DOAS measurements. *Atmospheric Chemistry and Physics, 17*, 10997–11023. doi:10.5194/acp-17-10997-2017

Sinreich, R., Merten, A., Molina, L., & Volkamer, R. (2013, June). Parameterizing radiative transfer to convert MAX-DOAS dSCDs into near-surface box-averaged mixing ratios. *Atmospheric Measurement Techniques, 6*, 1521–1532. doi:10.5194/amt-6-1521-2013

Vaquer, J. M. (2015). *Earth's climate response to a changing sun.* Cedex: European cooperation science and technology.

VOUNTAS, M., ROZANOV, V. V., & BURROWS, J. P. (1998, December). RING EFFECT: IMPACT OF ROTATIONAL RAMAN SCATTERING ON RADIATIVE TRANSFER IN EARTH'S ATMOSPHERE. *Journal of Quantitative Spectroscopy and Radiative Transfer, 60*, 943–961. doi:10.1016/s0022-4073(97)00186-6

Wikipedia Contributors. (2024, October 21). *Beer-Lambert Law*. Retrieved from https://en.wikipedia.org/w/index.php?title=Beer%E2%80%93Lambert_law&oldid=125102978

Wikipedia contributors. (2024, September 17). Beer–Lambert law. In Wikipedia, The Free Encyclopedia. Retrieved 10:24, September 26, 2024, from https://en.wikipedia.org/w/index.php?title=Beer%E2%80%93Lambert_law&oldid=1246134116.

Wikipedia contributors. (2024, September 24). *Sunlight. In Wikipedia, The Free Encyclopedia. Retrieved 10:46, September 26, 2024, from*. Retrieved from https://en.wikipedia.org/w/index.php?title=Sunlight&oldid=1230958260